

1
2
3
4 **Sensitivity of 24 h Forecast Dryline Position and Structure to Boundary Layer**
5 **Parameterizations in Convection-allowing WRF Model Simulations**
6
7

8
9 *Adam J. Clark^{1,2}, Michael C. Coniglio², Brice E. Coffey³, Greg Thompson⁴, Ming Xue^{5,6}, and Fanyou*
10 *Kong⁶*
11

12
13
14 ¹*Cooperative Institute for Mesoscale Meteorological Studies, The University of Oklahoma, Norman,*
15 *Oklahoma*

16 ²*NOAA/OAR National Severe Storms Laboratory, Norman, Oklahoma*

17 ³*Department of Marine Earth and Atmospheric Sciences, North Carolina State University, Raleigh,*
18 *North Carolina*

19 ⁴*National Center for Atmospheric Research, Boulder, Colorado*

20 ⁵*School of Meteorology, University of Oklahoma, Norman, Oklahoma*

21 ⁶*Center for Analysis and Prediction of Storms, University of Oklahoma, Norman, Oklahoma*
22
23
24

25 Submitted to
26 *Weather and Forecasting*
27 July 2014
28
29
30
31
32
33

34 * Corresponding author's address:

35 Adam J. Clark

36 National Weather Center, NSSL/FRDD

37 120 David L. Boren Blvd.,

38 Norman, OK, 73072

39 Email: adam.clark@noaa.gov

40 Phone: 405-325-6731
41
42
43
44

45 **Abstract**

46

47 Recent NOAA/Hazardous Weather Testbed Spring Forecasting Experiments have emphasized
48 the sensitivity of forecast sensible weather fields to how boundary layer processes are represented in the
49 Weather Research and Forecasting (WRF) model. Thus, since 2010, the Center for Analysis and
50 Prediction of Storms has configured at least three members of their WRF-model based Storm Scale
51 Ensemble Forecast (SSEF) system specifically for examination of sensitivities to parameterizations of
52 turbulent mixing, including the schemes MYJ, QNSE, ACM2, YSU, and MYNN (“PBL members”
53 hereafter). In post-experiment analyses, significant differences in forecast boundary layer structure and
54 evolution have been observed, and for pre-convective environments MYNN was found to have superior
55 depiction of temperature/moisture profiles.

56 This study evaluates the 24 h forecast dryline positions in the SSEF system PBL members
57 during the period April-June 2010-2012, and documents sensitivities of the vertical distribution of
58 thermodynamic and kinematic variables in near-dryline environments. Main results include: Despite
59 having superior temperature/moisture profiles as indicated by a previous study, MYNN was one of the
60 worst performing PBL members, exhibiting large eastward errors in forecast dryline position. During
61 2010-2011, a dry bias in the North American Mesoscale (NAM) model initial conditions largely
62 contributed to eastward dryline errors in all PBL members. An upgrade to the NAM model and
63 assimilation system in October 2011 apparently fixed the dry bias reducing eastward errors. Large
64 sensitivities of CAPE and low-level shear to the PBL schemes were found, which were largest between
65 1.0° and 3.0° degrees east of drylines. Finally, modifications to YSU to decrease vertical mixing and
66 mitigate its warm/dry bias greatly reduced eastward dryline errors.

67

68

69 **1. Introduction**

70 One of the biggest challenges facing the current generation of high-resolution numerical weather
71 prediction models is accurately forecasting the structure and evolution of the planetary boundary layer
72 (PBL), which has direct impacts on forecast sensible weather like low-level temperature, moisture, and
73 winds, as well as instability and convective initiation (e.g., Marshall et al. 2003; Roebber et al. 2004;
74 Hu et al. 2010; Coniglio et al. 2013). Because current models are still too coarse to resolve even the
75 largest turbulent eddies that vertically transport heat, moisture, and momentum in the PBL, these
76 transport processes must be parameterized, which can quickly introduce large forecast errors.

77 These PBL forecast uncertainties motivated a major emphasis of recent NOAA/Hazardous
78 Weather Testbed Spring Forecasting Experiments (SFEs; e.g., Clark et al. 2012), which involves
79 examining low-level thermodynamic and kinematic fields in Weather Research and Forecasting (WRF;
80 Skamarock et al. 2008) model simulations identically configured except for their scheme to
81 parameterize vertical effects of turbulent mixing¹. In fact, each year since 2010, the Center for Analysis
82 and Prediction of Storms (CAPS) has configured at least three members of their 4-km grid-spacing
83 Storm Scale Ensemble Forecast (SSEF) system specifically for examination of sensitivities to PBL
84 schemes, including the schemes Mellor-Yamada-Janjic (MYJ; Mellor and Yamada 1982, Janjic 2002),
85 quasi-normal scale elimination (QNSE; Sukoriansky et al. 2006), the Asymmetrical Convective Model
86 version 2 (ACM2; Pleim 2007), Yonsei University (YSU; Noh et al. 2003), and Mellor-Yamada,
87 Nakanishi, and Niino (MYNN; Nakanishi 2000, 2001; Nakanishi and Niino 2004, 2006). The MYNN,
88 MYJ, and QNSE schemes are considered “local” schemes because they use model fields only at
89 adjacent levels to determine the turbulent fluxes. The ACM2 and YSU schemes are considered “non-
90 local” schemes because they use model fields at a range of levels to simulate the effect of large eddies
91 in the convective PBL. Coniglio et al. (2013) provides additional details regarding the formulations of

¹ Although these schemes act at all model levels, they are commonly referred to as PBL schemes because most of the vertical mixing occurs within and near the PBL.

92 these schemes.

93 To date, the most thorough objective examination of PBL schemes used for SFEs was presented
94 in Coniglio et al. (2013), in which forecast thermodynamic variables were evaluated using radiosonde
95 observations upstream from deep convection. For forecasts valid during the evening, Coniglio et al.
96 (2013) found that the local schemes MYJ and QNSE produce PBLs that are generally too shallow/moist
97 while the non-local schemes ACM2 and YSU produce PBLs that are too deep/dry. The best results
98 were found for MYNN, which was nearly unbiased in PBL depth, moisture, and potential temperature,
99 with forecasts comparable to those from the operational North American Mesoscale Model (NAM;
100 Rogers et al. 2009). Coniglio et al. (2013) conclude that these results give confidence in the use of
101 MYNN over MYJ in pre-convective environments in convection-allowing WRF model configurations.
102 Similar positive results for the MYNN have led model developers working on the High Resolution
103 Rapid Refresh (HRRR; Alexander et al. 2013) model to switch from using the MYJ to the MYNN
104 scheme. Hu et al. (2010) also finds results similar to Coniglio et al. (2013), but only examining the
105 YSU, ACM2, and MYJ schemes.

106 Although MYNN has performed well in recent comparison studies, Coniglio et al. (2013) stress
107 that this superior performance should not necessarily translate into better forecasts of convection or
108 other aspects of simulations impacted by turbulent mixing like the positioning of drylines and fronts.
109 Thus, to build on the Coniglio et al. (2013) work, this study examines the same set of simulations, but
110 the PBL schemes are evaluated according to forecast dryline position. Additionally, thermodynamic
111 and kinematic variables associated with the dryline and near-dryline environment are examined, which
112 includes examination of dryline-relative composite vertical cross sections, soundings, and the dryline-
113 induced vertical circulations. Drylines are important because of their frequent role in convective
114 initiation over the southern high plains (e.g., Fujita 1958; Rhea 1966; Schaefer 1986). Furthermore,
115 knowledge of precise dryline position when present along with other environmental factors important

116 for severe weather (i.e., instability and vertical wind shear) is crucial for accurately delineating severe
117 weather risk areas by forecasters at agencies such as the Storm Prediction Center (SPC). Finally,
118 evaluating forecast dryline positions for different PBL schemes is also strongly motivated by Coffey et
119 al. (2013), who examined 24 h forecast dryline position errors in a 4-km grid-spacing version of the
120 WRF model run daily at the National Severe Storms Laboratory (NSSL), known as the NSSL-WRF.
121 Examining 116 dryline cases over a 5-year period, Coffey et al. (2013) found that the NSSL-WRF,
122 which uses the MYJ PBL scheme, had a systematic eastward bias of about 0.5° , which was present
123 across a wide spectrum of dryline cases. Thus, herein, we are particularly interested in whether the
124 WRF model simulations conducted by CAPS for the 2010-2012 SFEs exhibit this eastward bias and
125 whether the MYNN, which performed best in the Coniglio et al. (2013) evaluations, also exhibits
126 superior performance in forecast dryline position. The remainder of the study is organized as follows:
127 Section 2 presents information on WRF model configurations, analysis datasets, and dryline
128 identification methods, Section 3 presents results, which includes two case studies and aggregated
129 statistics over various sets of cases, and Section 4 provides a summary and conclusions.

130

131 **2. Data and methodology**

132 *a) WRF model configurations and analysis dataset*

133 Since 2007, CAPS has produced various versions of its SSEF system in support of annual
134 NOAA/Hazardous Weather Testbed SFEs (e.g., Xue et al. 2010; Kong et al. 2010, 2011). The basic
135 strategy in configuring the ensemble is to have one subset of members accounting for as many error
136 sources as possible to be used for ensemble forecasting, and another set of members configured for
137 examination of physics sensitivities, which has mainly involved examination of microphysics and PBL
138 schemes. Herein, forecasts from the 2010-2012 SFEs are examined. The 2010, 2011, and 2012 SFEs
139 were conducted 17 May – 18 June, 9 May – 10 June, and 7 May – 8 June, respectively, with SSEF

140 system forecasts becoming available about two weeks before the start dates of each year. The subset of
141 SSEF system members used in this study are configured identically, except for their PBL schemes
142 (“PBL members” hereafter). In two case study analyses, results from SSEF members with perturbed
143 initial conditions (ICs) and lateral boundary conditions (LBCs) along with mixed physics are also
144 shown.

145 During 2010, there were three PBL members that used the schemes MYJ, MYNN, and QNSE.
146 During 2011, six PBL members were run that included the PBL members from 2010, as well as ACM2,
147 YSU, and another experimental version of YSU provided by Greg Thompson of NCAR (hereafter, the
148 modified YSU is referred to as YSU-T). Previous subjective evaluations of numerous model
149 simulations using YSU by SFE participants found a dry and warm bias in the PBL in typical late spring
150 mid-continental US convective cases that included drylines forecast too far east. These features had
151 been noted during prototype real-time summer forecast experiments for a number of prior years.
152 Therefore, some attempt to combat these perceived biases was attempted, which included the set of
153 code changes summarized in Table 1.

154 Finally, during 2012, there were five PBL members, which consisted of the same PBL members
155 from 2011, except for the YSU-T member. Other than the WRF model version (3.1.1, 3.2.1, and 3.3.1
156 for 2010, 2011, and 2012, respectively), all other aspects of the model configurations, which are
157 summarized in Table 2, were the same for all three years examined. To our knowledge, there are no
158 major changes between the model versions that would have a significant effect on our results.

159 The WRF model forecasts used 4-km grid-spacing with 51 vertical levels and were initialized on
160 weekdays at 0000 UTC and integrated 30 or 36 h over a CONUS domain during the period late-April
161 through mid-June. For this study, only the 24 h lead-time forecasts are considered. ICs and LBCs (3-h
162 updates) were from the 12-km grid-spacing NAM model analyses and forecasts, respectively.
163 Reflectivity data from up to 140 Weather Surveillance Radar-1988 Doppler (WSR-88Ds) and other

164 traditional data, such as surface observations, rawinsondes, and wind profilers, were assimilated into
165 ICs of the simulations using the Advanced Regional Prediction System (ARPS) three-dimensional
166 variational data assimilation (3DVAR; Xue et al. 2003; Gao et al. 2004) and cloud analysis (Xue et al.
167 2003; Hu et al. 2006) system. Another member that did not use the 3DVAR system is also examined in
168 some of the case study analyses. IC perturbations were derived from evolved (through 3 h)
169 perturbations of 2100 UTC initialized members of NCEP's Short-Range Ensemble Forecast (SREF)
170 system (Du et al. 2006) and added to the control member ICs. For each perturbed member, the SREF
171 member used for the IC perturbations was also used for the LBCs.

172 For identifying observed dryline locations, the 20-km grid-spacing Rapid Update Cycle (RUC)
173 model analyses from NCEP (Benjamin et al. 2004a, b) were used following Coffey et al. (2013). These
174 analyses are generated using hourly intermittent 3DVAR data assimilation cycles in which recent
175 observations from various sources (e.g., wind profilers, radar, aircraft, METARs, satellites, etc.) are
176 assimilated using the previous 1-h RUC model forecasts as the background. On 1 May 2012 the Rapid
177 Refresh replaced the RUC as the NOAA hourly-updated assimilation/modeling system at NCEP
178 (Brown et al. 2012). Given the frequent data assimilation cycles and relatively dense network of
179 surface observations over the southern plains where drylines are most common, it is expected that the
180 RUC analyses accurately and reliably depict the observed dryline positions. The accuracy of the
181 dryline positions depicted by RUC analyses was confirmed through some simple comparisons between
182 dryline positions manually determined from surface data charts and the dewpoint fields in the RUC (not
183 shown). Coniglio (2012) documented a slight moist bias near the surface in RUC analyses (~ 0.7 K)
184 with no systematic temperature biases. However, there is no reason to believe that these small moisture
185 biases would affect the dryline position, which is determined by dewpoint differences many times
186 greater in magnitude than the moist biases in the RUC.

187

188 *b) Dryline identification*

189 In the 24 h PBL member forecasts and corresponding RUC analyses, dryline positions were
190 determined using the manual identification procedure developed by Coffey et al. (2013). The main
191 criterion for dryline classification was an unambiguous boundary between relatively moist and dry air
192 with along boundary length scales of $O(100)$ km. Moisture boundaries were identified using the 2-m
193 specific humidity field and it was required that at some point along the boundary the specific humidity
194 gradient magnitude was at least $3 \text{ g kg}^{-1} (100 \text{ km})^{-1}$. In addition, the 2-m temperature field was used to
195 distinguish drylines from cold fronts. Moisture boundaries clearly resulting from convective outflow
196 were not considered. Finally, a shift in the 10-m wind direction from a dry to moist source region was
197 required. The existence of this shift was subjectively determined. Dryline identification was performed
198 over the domain bounded by 30° N to 43° N and -106° W to -90° W longitude.

199 For cases in which dryline criteria were met, a Grid Analysis and Display System (GrADS;
200 <http://www.iges.org/grads/>) script was used to manually draw a series of points along the axis of
201 maximum specific humidity gradient magnitude. Straight-line segments connecting these points
202 composed the dryline, and corresponding latitude/longitude coordinates were output to files for
203 subsequent analysis. To compute average dryline longitude, the midpoint longitude of each line
204 segment composing the dryline was computed. Then, weights were assigned to each midpoint
205 longitude based on the ratio of the corresponding segment length to that of the entire dryline, and the
206 average dryline longitude was computed as the weighted average of the midpoint longitudes. For
207 reference, at the northern-most, middle, and southern-most latitudes of the analysis domain, 1°
208 longitude corresponds to 81.3, 89.4, and 96.3 km, respectively.

209 To account for the differences in scales between the 4-km grid-spacing forecasts and the 20-km
210 grid-spacing RUC analyses, a Gaussian weighted filter was used to dampen wavelengths below 120 km
211 in the specific humidity field before computation of gradient magnitudes. Coffey et al. (2013) found

212 that application of this filter smoothed out fine-scale structures in the gradient fields while retaining and
213 oftentimes emphasizing the dryline position, which was especially important for the higher resolution
214 WRF model simulations. For further details on the procedure and examples of its application, see
215 Coffe et al. (2013).

216 Over the period late-April through mid-June 2010-2012, 40 cases in which drylines were present
217 in all PBL members and the RUC analyses were identified. Because the SSEF system was not run on
218 weekends, these 40 cases do not represent all the dryline cases that occurred during this period. The 40
219 cases include 10 during 2010 (30 April; 7, 11-13, 20, 22, and 25 May; and 12 and 18 June – drylines
220 were present at 0000 UTC on dates listed), 14 during 2011 (30 April; 10-13, 18-21, 24-25, and 28-31
221 May; and 9 June) and 16 during 2012 (26 and 28 April; 1-2, 4-5, 19, 23-26, 28, and 30-31 May; 10 and
222 11 June). Because the PBL members from all three years include the MYJ, MYNN, and QNSE
223 schemes, there is a sample size of 40 cases for comparing these members. The PBL schemes ACM2
224 and YSU were only run during 2011 and 2012, so there is a sample size of 30 cases for comparing these
225 members, and YSU-T was only run during 2011 for a sample size of 14 cases.

226

227 **3. Results**

228 *a. Example cases*

229 Figures 1-5 illustrate dewpoint fields and dryline positions for two representative cases, which
230 were chosen because they depict drylines associated with a range of severe weather risks [e.g., slight
231 risk on 12 May 2010 (Fig. 1), and high risk on 24 May 2011 (Fig. 4)]. Furthermore, as will be shown in
232 subsequent analyses, there was an overall eastward bias in forecast dryline positions, and both of these
233 cases contain this eastward bias.

234

235 1) 12 MAY 2010

236 A cut off mid-tropospheric low embedded within a broad mid-tropospheric trough progressed
237 slowly eastward 12-13 May covering roughly the western half of the US. Downstream of the trough, a
238 broad region of southwesterly 500-hPa winds > 50 knots extended from northern Texas and western
239 Oklahoma, into Kansas, northern Missouri, eastern Nebraska and Iowa (not shown). At the surface, a
240 frontal boundary was stretched across northern Missouri, eastern Kansas, and northwest Oklahoma, and
241 into the Texas panhandle, with a dryline extending south across western Texas (Fig. 1d). Because of
242 sufficient deep-layer vertical shear and convective instability for severe storms east of the frontal
243 boundary and dryline, SPC issued a slight risk for much of this region. Around 2000 UTC a broken line
244 of storms formed in south central Kansas along the frontal boundary producing a couple tornadoes and
245 numerous severe hail and wind reports (Fig. 1e). By 2200 UTC another broken line of storms that
246 produced severe hail and a few tornadoes had formed along the northern part of the dryline in the
247 eastern Texas panhandle. Finally, around 0200 UTC another round of storms formed in the Texas
248 panhandle near the triple-point (i.e., intersection of warm/dry, warm/moist, and cool/dry air-masses to
249 the west, east, and north of the dryline, respectively) as the frontal boundary began to move south.

250 The dryline position in this case (along with the frontal boundary) played an important role in
251 where storms and associated severe weather occurred and the particularly large 24 h forecast dryline
252 position errors (e.g., Fig. 1e) could have mislead forecasters into believing the severe weather threat
253 was farther east than in reality. The easternmost extent of the dryline identified in the RUC analyses at
254 0000 UTC 13 May was about -101.5° W, while that of the forecast drylines was about -98.0° W. The
255 average eastward errors for MYJ, QNSE, and MYNN were 1.9° , 2.1° , and 2.8° , respectively. There
256 were also very noticeable differences in the northernmost extent of the forecast and observed drylines,
257 which was related to the position of the SW to NE oriented frontal boundary to which the dryline was
258 attached forming the triple-point. The farther east the dryline mixed, the farther northeast along the
259 frontal boundary the triple-point became positioned. In the MYJ and QNSE simulations (Figs. 1a and

260 1c, respectively), the frontal boundary position was well forecast, thus, the position of the triple-point
261 was mostly only affected by the eastward dryline position error. However, in the MYNN simulations
262 (Fig. 1b), the frontal boundary was positioned too far north exacerbating the northward position error of
263 the forecast triple-point position in east-central Nebraska, which was about 400 km from the observed
264 triple-point in the Texas panhandle. The 24 h forecast dryline positions for non-PBL SSEF system
265 members (grey lines in Fig. 1e) also incorrectly simulated the westward extent of the observed dryline
266 position.

267 For further insight on the dryline position errors and their evolution in the 24 h forecast, a time-
268 longitude plot of observed and forecast dryline positions at 34° N is shown in Fig. 1f. As in the spatial
269 plots, the drylines in time-longitude space were manually identified using the axis of maximum specific
270 humidity gradient magnitude. During the first 9 h of the forecast (bottom of 1f), the dryline in the RUC
271 analyses retreated westward. Then, after 0900 UTC, the RUC dryline moved eastward until 1800 UTC
272 after which it retreated slightly westward again. This east-west diurnal variability is typical of drylines
273 and the forecast dryline east-west diurnal variation follows a similar pattern. However, there is a
274 surprisingly large difference in the dryline longitude at the forecast initialization time with the RUC
275 dryline about 0.75° west of the SSEF member drylines. This difference can be seen at the bottom of
276 Fig. 1f, as well as by comparing the 2-m dewpoint from the RUC analysis valid 0000 UTC 12 May
277 (Fig. 2a) to that of MYJ without (Fig. 2b) and with (Fig. 2c) the 3DVAR data assimilation and cloud
278 analysis (the MYJ without data assimilation is just the downscaled NAM analysis). It appears that this
279 initial offset, combined with the forecast drylines not retreating far enough west during 0 – 9 h forecast
280 period and then mixing too far east during the 9 – 18 h forecast period, led to the very large errors in the
281 24 h forecast.

282 Furthermore, the MYJ forecasts were generally much drier than corresponding RUC analyses in
283 much of northern Mexico, far southwest Texas, and eastern New Mexico, which can be seen from 2-m

284 dewpoint difference plots between MYJ and RUC (Figs. 2d, i, n, s, x, and γ). In these plots, MYJ
285 without 3DVAR data assimilation is used because it was found that the impact of the 3DVAR system
286 on the 2-m dewpoint field greatly diminishes just 12 h into the forecast, which can be seen in the 2-m
287 dewpoint difference plots between MYJ with and without the 3DVAR data assimilation and cloud
288 analysis (Fig. 2e, j, o, t, y, and δ). Notice that the 3DVAR system adds a large area of increased
289 moisture over northern Mexico/southwest Texas (Fig. 2e), but this increased moisture quickly
290 dissipates. The increased moisture there suggests that there were observations supporting its presence,
291 but that the overriding influence of the NAM ICs/LBCs eliminated its influence later in the forecast.
292 Thus, we suspect that a dry bias in the NAM also contributed to the large forecast dryline errors.
293 Further supporting the dry NAM bias, Figure 3b shows the 2-m dewpoint from the 0000 UTC 12 May
294 NAM analysis, with dots overlaid at the locations of surface observations. The size and color of the
295 dots indicates the difference between the observations and the nearest grid-point of the NAM analysis.
296 Along and west of the moisture gradient there is a particularly noticeable dry bias in the NAM analysis,
297 with a mean dewpoint difference between the observations and NAM analysis of -1.67° C. The RUC
298 analysis 2-m dewpoint (Fig. 3a) is a better match with observations, but with a slight moist bias (mean
299 dewpoint difference between observations and RUC analysis is 0.41° C).

300

301 2) 24 MAY 2011

302 A high amplitude mid-tropospheric short-wave trough moved rapidly eastward into the southern
303 high plains during the afternoon of 24 May with an associated dryline that had progressed to western
304 Oklahoma by 2100 UTC. The air mass east of the dryline was extremely unstable and co-located with
305 strong upper-level flow that veered with height, creating favorable conditions for severe weather
306 including strong long-track tornadoes and large hail. Accordingly, SPC issued a “high risk” for severe
307 weather in their Day 1 outlooks (Fig. 4h). Around 1900 UTC, the first dryline-initiated storms formed

308 in southwest Oklahoma and quickly moved northeast. By 2100 UTC, storm coverage along the dryline
309 had increased dramatically with a broken line of supercells stretching along and just east of the dryline
310 from south central Kansas, through western Oklahoma, and into north Texas (not shown). Some of the
311 supercells produced violent, long-track tornadoes.

312 Again, the dryline position played an important role in where storms and associated severe
313 weather occurred, and, similar to 12 May 2010, there were particularly large 24 h forecast dryline
314 position errors (e.g., Fig. 4h). The easternmost extent of the dryline identified in the RUC analyses at
315 0000 UTC 25 May was about -99.0° W, while SSEF member drylines extended east as far as -96.75°
316 W. From smallest to largest, the average eastward errors for YSU-T, YSU, ACM2, MYJ, QNSE, and
317 MYNN were 0.8° , 1.0° , 1.2° , 1.2° , 1.3° , and 1.6° , respectively. Similar to 12 May 2010, in addition to
318 having the largest eastward dryline position errors, the MYNN also placed the triple point much farther
319 north into central Kansas relative to observations and the other PBL members.

320 The time-longitude plot of observed and forecast dryline positions at 34° N (Fig. 4i) shows that,
321 unlike 12 May 2010, the dryline longitude at the initialization time in the RUC and NAM analyses lines
322 up quite well. During the first 15 h of the forecast, the dryline in the RUC analyses slowly moved
323 westward, with a brief excursion to the east and retreat back to the west between 1200 and 1500 UTC.
324 Then, between 1500 and 2100 UTC the RUC dryline mixed eastward, and remained virtually stationary
325 from 2100 to 0000 UTC. The dryline longitudes in the PBL members line up well with the RUC
326 analyses up until about 6 h into the forecast. Then, instead of continuing to slowly move westward, the
327 PBL member drylines begin to move eastward and by 1500 UTC there are already significant eastward
328 position errors relative to the RUC analyses. After 1500 UTC, the RUC analyses and PBL member
329 drylines mix eastward at about the same speed, but instead of stopping at 2100 UTC as in the RUC
330 analyses, the forecast drylines in all the PBL members continue to mix east until 0000 UTC.

331 Comparing the 2-m dewpoint from the RUC analysis valid 0000 UTC 24 May (Fig. 5a) to that

332 of MYJ without (Fig. 5b) and with (Fig. 5c) the 3DVAR data assimilation and cloud analysis system,
333 there is a general dry bias in the MYJ relative to the RUC over far southwest Texas and the Texas
334 panhandle as well as New Mexico (see difference plots in Fig. 5d). Also, the southern portion of the
335 dryline in the RUC analysis has a tighter moisture gradient and extends farther west relative to the MYJ
336 analyses, which is reflected in the difference plots by the adjacent axes of positive and negative
337 moisture differences in west-central Texas (Fig. 5d). These negative moisture differences can be
338 tracked through time (Figs. 5d, i, n, s, and x), thus, similar to the 12 May 2010 case, we suspect that the
339 dry bias in the NAM analysis contributed to the dryline errors.

340

341 *b) Aggregate Dryline Statistics*

342 For a robust statistical analysis of average dryline position errors, Fig. 6 shows box-plots
343 constructed using the distributions of average longitudinal dryline errors in the PBL members. For the
344 three PBL members that could be compared from the 2010-2012 sample of 40 cases (top three box plots
345 in Fig. 6), there was a clear eastward bias in 24 h forecast dryline position with the mean eastward error
346 of all three significantly different from zero (indicated by pink shading in Fig. 6). In fact, the entire
347 interquartile range in all three box-plots is greater than zero. The QNSE and MYJ members had similar
348 distributions with median eastward errors just above 0.5° , while the MYNN had a median eastward
349 error of about 0.90° . From the box-plots on the right-hand-side of Fig. 6, the differences relative to
350 MYJ for QNSE were distributed around zero, while for MYNN the median difference was about 0.30° ,
351 and there was only one case in which the MYNN had a dryline west of that from MYJ.

352 For the five PBL members for the 2011-2012 sample of 30 cases, again, there was a clear
353 eastward bias in forecast dryline position, with median eastward errors ranging from about 0.40° in
354 QNSE and MYJ to about 0.60 - 0.75° in YSU, MYNN, and ACM2. MYNN and ACM2 drylines tended
355 to be furthest east relative to MYJ, while YSU drylines were to the east, but not as far as MYNN and

356 ACM2. Relative to MYJ, the mean differences in average dryline longitude for MYNN, ACM2, and
357 YSU were all significantly different than zero.

358 Finally, for the six PBL members for the 2011 sample of 14 cases, the eastward bias was present
359 and was the largest among the three sets of cases examined. However, the relative differences among
360 the PBL members are similar to the other sets of cases. The dryline errors for the YSU-T member,
361 which was only run during 2011, were particularly notable because they tended to be west relative to
362 the MYJ member, which was the only scheme for which this was the case in the entire dataset. The
363 average dryline differences between the YSU and YSU-T member were statistically significant,
364 however, the YSU-T average dryline differences relative to MYJ were not statistically significant.

365

366 *c) Impact of IC errors on forecast dryline errors*

367 For 12 May 2010 and 24 May 2011, the eastward dryline errors seemed closely related to a dry
368 bias in the NAM ICs. To further investigate whether IC errors played a role in dryline errors for the
369 other cases, average 2-m dewpoint biases were computed over the region -105° W to -99° W and 29° N
370 to 39° N. This area was chosen because it appeared to be where dry biases were largest in the case
371 studies. The 2-m dewpoint errors were computed using surface observations from the Meteorological
372 Assimilation Data Ingest System (MADIS; Miller et al. 2005, 2007). For each surface observation
373 within the bounded region, the difference between the 2-m dewpoint of the MADIS observation and
374 that of the nearest grid-point of the NAM ICs was computed. Then, the bounded region was divided
375 into 1.0° longitude x 1.0° latitude squares, and average differences were computed over each square so
376 that areas with more dense observations would not be given disproportionate weight. Finally, an
377 average 2-m dewpoint error was computed by averaging over all the 1.0° x 1.0° squares.

378 To test the impact of the NAM 2-m dewpoint errors on the forecast dryline positions, scatter
379 plots were created in Figure 7 by plotting the average error over the bounded region against the average

380 longitudinal dryline position error for each case. The scatter-plots were created only for the members
381 that were available from all 40 cases. The correlation coefficients were computed using the *cor.test()*
382 function from the R statistical software package (R Development Core Team 2014). The correlation
383 coefficients were -0.44, -0.46, and -0.48, for the MYJ, QNSE, and MYNN members, respectively, all of
384 which were highly significant with p-values ≤ 0.005 . Best-fit lines computed using linear regression are
385 also shown in Figure 7. Thus, there is strong evidence that systematic errors in the 2-m dewpoint
386 analysis of the NAM explain much of the forecast dryline position errors. Physically, this makes sense
387 – a drier initial state should result in greater sensible heat flux and stronger vertical mixing, which
388 would tend to push the dryline farther east. It is also possible that the dryline itself is too far east in the
389 NAM analyses, which should also contribute to eastward position errors later in the forecast.

390 The MYJ and QNSE contained a very similar relationship between NAM IC 2-m dewpoint bias
391 and forecast dryline error (Fig. 7d), which is not surprising since it was found in the previous sections
392 these two schemes behave very similarly. For the MYNN, the slope of the best-fit line was almost
393 identical to that of MYJ and QNSE, but shifted to greater dryline errors by about 0.30° , consistent with
394 results in Fig. 6. Of particular interest in Fig. 7d is the longitudinal dryline error for a dewpoint bias of
395 zero (i.e., the y-intercept). For the MYJ and QNSE, the y-intercept is about 0.30° , while for MYNN it
396 is about 0.60° . This means that, even when the NAM IC 2-m dewpoint is unbiased, there is still a
397 systematic eastward bias in the forecast dryline positions, which is most pronounced in MYNN. The
398 dryline error present when the 2-m dewpoint bias is near zero can be attributed to the PBL schemes or
399 other aspects of the WRF model formulation.

400

401 *d) Dryline position errors by year*

402 In Figure 8, the average 2-m dewpoint errors for each year are shown over the bounded region
403 described in the previous section, along with corresponding box-plots of dryline errors for MYJ, QNSE,

404 and MYNN. The average 2-m dewpoint errors for 2010 and 2011 were -2.05° and -1.27° C,
405 respectively, and both years had clear eastward biases in 24 h forecast dryline position. However, in
406 2012, the 2-m dewpoint biases were near zero, with corresponding eastward dryline position errors in
407 all three PBL members that were noticeably smaller than in 2010 and 2011. In MYJ and QNSE, the
408 median dryline errors were near zero during 2012, while in MYNN they were about 0.60° .

409 It is likely that the reduction in the 2-m dewpoint bias of the NAM ICs was related to a major
410 upgrade of the NAM model and data assimilation system that occurred in October of 2011. For this
411 upgrade, a new modeling framework known as the NOAA Environmental Modeling System (NEMS)
412 was implemented and modifications were made to the NAM data assimilation system (NDAS) that uses
413 the Gridscale Statistical Interpolation (GSI) analysis. The NDAS changes included assimilation of new
414 observations from numerous different platforms, as well as updating the 2-m temperature and dewpoint
415 fields (before the update, the 2-m temperature/moisture fields were simply the first guess from the
416 previous model cycle). A summary of these changes can be found at the URL:
417 http://www.nws.noaa.gov/os/notification/tin11-16nam_changes_aad.htm.

418

419 *e) Vertical structure of drylines and near-dryline environment*

420 To further investigate how the various PBL schemes depict the PBL and how these depictions
421 may be related to the dryline position errors, dryline-relative composite vertical cross sections of the
422 near-dryline environment were constructed for each PBL member. At 0.15° latitude increments along
423 the dryline, vertical cross-sections of selected fields are extracted up to model level 35 (~ 200 mb) from
424 2.0° west of the dryline to 4.0° east of the dryline. Then, a composite cross section for each case is
425 taken by averaging over all these individual cross sections, and a single composite cross section for
426 each PBL member is taken by averaging the composites over all the cases. Composite vertical cross
427 sections of specific humidity, temperature, pressure, vertical velocity, and wind magnitude were

428 examined. Figure 9 illustrates how this procedure was implemented for MYJ and MYNN forecasts
429 initialized 10 May 2010. The composite cross sections smooth out some of the tight vertical gradients
430 in specific humidity that can be seen in the individual cross sections, but the main characteristics of the
431 PBL are retained. For example, comparing Fig. 9e (MYJ) to Fig. 9j (MYNN) it is easily seen that the
432 MYJ has a PBL that is shallower and moister than the MYNN.

433 Vertical cross-section composites from each PBL member available during the 2011-2012
434 period (30 cases) are shown in Figure 10. This specific period was chosen for examination because
435 there is a large sample for which 5 out of the 6 PBL members were available. For specific humidity
436 (Figs. 10a-e), the vertical extent of the dryline, as well as the interface between the PBL and elevated
437 mixed layer, stand out very clearly. To more clearly illuminate differences among the members, Figs.
438 10f-i show differences in specific humidity relative to MYJ. Differences are shown relative to MYJ
439 because it is arguably the most popular PBL scheme and it has been used in the control member of the
440 SSEF system since 2007. From the difference plots it is clear that the vertical distribution of moisture
441 west of the dryline is very similar in each of the five PBL members. However, east of the dryline in the
442 moist sector there are much more noticeable differences in the vertical moisture distribution. QNSE has
443 the smallest moisture differences relative to MYJ, which is not surprising because the two schemes are
444 formulated similarly.

445 Specific humidity differences relative to MYJ in MYNN, ACM2, and YSU are much larger than
446 those of QNSE and all exhibit a very similar pattern. In the layer closest to the ground, these members
447 are drier than MYJ, while between about 850 and 700 hPa they are moister. This pattern is consistent
448 with a deeper and overall drier PBL than MYJ and closely matches the results presented in Fig. 10 of
449 Coniglio et al. (2013). The differences are also dependent on the distance from the dryline (i.e., x-axis
450 in Figure 10), in particular, the largest positive moisture differences centered between 850 and 700 mb
451 occur between 1.0° and 3.0° east of the dryline. This result is consistent with the strength of the

452 capping inversion increasing with eastward distance from the dryline, which usually occurs because the
453 areas well east of the dryline are not impacted by the dryline-induced vertical circulation. Also,
454 oftentimes when the dryline is linked to a synoptic scale weather system, areas farther east of the
455 dryline are less influenced by large-scale dynamical processes (e.g., differential vorticity advection) that
456 can contribute to eroding capping inversions. When a stronger capping inversion exists, differences in
457 the PBL depth can result in very large moisture differences where levels in one member are within the
458 dry/stable cap and the same levels in another member are within the well-mixed PBL.

459 In the temperature composites (Figs. 10j-n) the dryline is not reflected as obviously as in the
460 specific humidity composites, however, there is a clear temperature change from warmer to cooler
461 across the dryline boundary, which is a well known characteristic of drylines caused by differences in
462 sensible heat flux. In the difference plots (Figs. 10o-r), QNSE has almost undetectable differences in
463 temperature relative to MYJ. However, much more noticeable differences exist in the other three PBL
464 members and, similar to the specific humidity composites, the patterns in these members have some
465 similarities. In the MYNN, ACM2, and YSU the largest negative temperature differences relative to
466 MYJ occur in the 850 to 700 mb layer about 2.0° to 3.5° east of the dryline. These negative differences
467 reflect levels where there was a capping inversion present in MYJ, while the capping inversion in the
468 MYNN, ACM2, and YSU was weaker or completely eroded. Positive temperature differences
469 generally existed in the layer adjacent to the ground. In the MYNN, the positive differences were
470 largest from 0 to 1 degrees longitude east of the dryline, in ACM2 the positive differences were largest
471 within a deep layer from 0 to 2 degrees longitude west of the dryline, and in YSU the positive
472 differences were relatively homogeneous, but tended to be slightly larger east of the dryline. The
473 results here are consistent with an overall deeper and warmer PBL in the MYNN, ACM2, and YSU
474 members relative to MYJ, and once again similar to findings of Coniglio et al. (2013).

475 The differences in the dryline-relative vertical cross sections of temperature and specific

476 humidity are consistent with the differences in average forecast dryline positions errors for the different
477 PBL members. The tendency for some of the schemes to produce warmer/drier/deeper PBLs implies
478 stronger vertical mixing, which in turn should result in a farther eastward dryline position because
479 vertical mixing is usually the dominate process governing dryline movement. For example, MYJ and
480 QNSE depict shallower/moister/cooler PBLs relative to the other members corresponding to more
481 westward dryline positions, while ACM2, MYNN, and YSU depict deeper/drier/warmer PBLs
482 corresponding to more eastward dryline positions. However, the relationship between PBL
483 depth/moisture/temperature and dryline position is not perfect. For example, YSU tends to depict a
484 deeper/drier/warmer PBL than MYNN, but the average YSU dryline position errors are not as far east
485 as MYNN.

486 In the wind magnitude composites (Figs. 10s-w), wind speeds are greater in the PBL east of the
487 dryline line than they are to the west in all 5 PBL members. Also, there is an extension of faster wind
488 speeds from the upper-level jet just above and to the east of the upward branch of the dryline-induced
489 vertical circulation. This downward extension of faster wind speeds coincides with an area of
490 downward motion (not shown) related to the dryline-induced vertical circulation, thus, it is likely
491 caused by downward momentum transport (the vertical circulations are examined in a subsequent
492 section). In the difference plots (Figs. 10o- α), the main difference relative to MYJ in the QNSE member
493 is slightly faster wind speeds between 925 and 850 mb to the east of the dryline. In the YSU, ACM2,
494 and MYNN, wind speeds are slightly slower than MYJ in the lowest levels up to about 850 mb east of
495 the dryline. Additionally, these three members also have areas above the PBL where wind speeds are
496 slower than MYJ, and a small layer between 850 and 700 hPa roughly co-located with the top of the
497 PBL where wind speeds are faster than MYJ. The weaker PBL winds in MYNN, ACM2, and YSU are
498 likely the result of more vertical mixing/turbulence in these schemes relative to MYJ.

499 To evaluate the impact of modifications designed to decrease vertical mixing made to YSU in

500 the YSU-T member, Figure 11 shows dryline-relative composite vertical cross sections for the MYJ,
501 YSU, and YSU-T PBL members for 2011 (14 cases), which was the only period over which YSU-T
502 was run. Recall, the eastward dryline position errors for YSU-T were noticeably less than YSU, and
503 during 2011 YSU-T was the only PBL member with eastward dryline position errors smaller than MYJ
504 (Fig. 6). Thus, one might expect that weaker vertical mixing in the YSU-T member results in a
505 shallower/cooler/moister PBL than YSU and MYJ. Interestingly, this is not the case – the difference
506 plot shown in Figs. 11f indicates that specific humidity differences between YSU and YSU-T are very
507 small and Figs. 11d-e show that both YSU and YSU-T have similarly deeper/drier PBLs relative to
508 MYJ. Similarly, in the temperature composites, Fig. 11i indicates that YSU and YSU-T had only very
509 small differences east of the dryline, and west of the dryline, YSU-T was slightly cooler than YSU.
510 Finally, in the wind magnitude composites (Figs. 11m-r), YSU-T had slightly weaker winds in the PBL
511 1.0° to 2.0° immediately east of the dryline. Given the small differences between YSU and YSU-T, it is
512 difficult to explain why the differences in forecast dryline positions were so dramatic. The cooler
513 temperature profiles west of the dryline along with weaker winds east of the dryline in YSU-T are
514 consistent with less vertical mixing in YSU-T; however, these were only very subtle differences.
515 Further investigation beyond the scope of this study is needed to better explain the differences in
516 forecast dryline position in YSU and YSU-T.

517

518 *f) Composite sounding analysis*

519 To complement the dryline-relative composite cross-sections, 24 h composite forecast soundings
520 are presented in Figure 12. The composite soundings were constructed by finding an “anchor point”
521 following the dryline 1.0° south from its northernmost latitude. Then, average dewpoint, temperature,
522 and winds were taken from 1.0° west, and 0.5° , 1.0° , 1.5° , 2.0° , and 2.5° east of this anchor point to
523 construct the composite soundings for each member at each of these distances. Additionally, surface-

524 based convective available potential energy (CAPE), convective inhibition (CIN), and storm relative
525 helicity in the lowest 100 and 300 hPa layer (SRH1 and SRH3, respectively) were computed from the
526 composite profiles. Rather than average over the north-south direction as was done to create the
527 composite cross sections, the composite soundings are constructed relative to only one point on the
528 northern section of the dryline in order to sample the area of the moist sector most likely to be within an
529 environment favorable for severe weather. Environments immediately to the east of northern portions
530 of the dryline tend to be associated with greater deep layer wind shear and smaller convective inhibition
531 relative to southern portions of the dryline because of their closer proximity to synoptic scale weather
532 systems and their associated dynamics. The composite soundings are presented to provide perspective
533 on how sensitive products relevant to severe weather forecasting are to the PBL schemes and how this
534 sensitivity changes depending on distance from the dryline.

535 In the post-dryline environment at 1.0° west of the dryline (Fig. 12a), temperature profiles in all
536 members are virtually identical with dry adiabatic lapse rates extending up to near 600 hPa. The
537 dewpoint profiles are more variable than temperature, with QNSE and MYJ slightly moister than the
538 other schemes up to about 800 hPa. As expected in the post-dryline environment, all members have
539 zero CAPE and very small values of SRH because the wind profiles are mainly uni-directional. Within
540 the moist sector at 0.5° east of the dryline (Fig. 12b), again, temperature profiles are very similar among
541 the 5 PBL members with more variability in the dewpoint profiles. Average CAPE values range from
542 1506 J/kg in the YSU member to 1948 J/kg in the QNSE member. MYJ and QNSE have higher CAPE
543 than the other schemes because of a moister dewpoint profile in the lowest ~ 75 hPa. Small variability
544 was present in values of SRH1 and SRH3 with SRH1 ranging from $86 \text{ m}^2\text{s}^{-2}$ in YSU to $110 \text{ m}^2\text{s}^{-2}$ in
545 MYJ and SRH3 ranging from $190 \text{ m}^2\text{s}^{-2}$ in QNSE to $222 \text{ m}^2\text{s}^{-2}$ in ACM2. The small variability in SRH
546 is reflected in the similar hodographs at the bottom left of Fig. 12b. At 1.0° , 1.5° , 2.0° , and 2.5° east of
547 the dryline, larger differences among the schemes begin to emerge. At these distances, CAPE values

548 are much higher in MYJ and QNSE than ACM2, YSU, and MYNN, with the differences most
549 pronounced at 1.5° east of the dryline where CAPE values were just above 2250 J/kg in MYJ and
550 QNSE, and ranging from about 1500 to 1750 J/kg in MYNN, YSU, and ACM2. The larger CAPE in
551 MYJ and QNSE was mainly the result of the moister low-level dewpoint profiles in these members.
552 Additionally, at distances farther east, the temperature profiles begin to exhibit more variability
553 especially centered around the 800 hPa level where the MYJ and QNSE members are noticeably
554 warmer than YSU, ACM2, and MYNN, which is consistent with their tendency to have more
555 pronounced capping inversions. Furthermore, at distances 1.0° east of the dryline and greater, values of
556 SRH exhibit more variability. The faster PBL wind speeds in MYJ, and especially in QNSE (e.g., Figs.
557 10x- α), result in more “looped” hodographs and higher SRH relative to ACM2, MYNN, and YSU. For
558 example, at 1.0° east of the dryline (Fig. 12c), SRH1 was 108 and 155 m^2s^{-2} in MYJ and QNSE,
559 respectively, compared to 72, 86, and 87 m^2s^{-2} in MYNN, ACM2, and YSU, respectively.

560 Similar to the analysis of the composite vertical cross sections, to evaluate the impact of
561 modifications made to YSU in the YSU-T member, Figure 13 shows composite soundings for the YSU
562 and YSU-T PBL members for 2011 (14 cases). In general, the temperature profiles at all distances from
563 the dryline are very similar, and the dewpoint profiles exhibit slightly more variability with the main
564 differences being a tendency for slightly more moist dewpoint profiles in lower levels in the YSU.
565 Differences in CAPE were less than 150 J/kg and stronger low-level winds in YSU resulted in much
566 larger values of SRH at 0.5° and 1.0° east of the dryline.

567

568 *g) Strength of vertical dryline-induced circulation*

569 Several observational and modeling-based studies of the dryline have found that virtual potential
570 temperature gradients across the dryline result in a baroclinic solenoidal circulation (e.g., Parsons et al.
571 1991; Ziegler and Hane 1993; Ziegler et al. 1995; Hane et al. 1997; Atkins et al. 1998; Ziegler and

572 Rasmussen 1998). Maximum vertical velocities within the upward branch of this circulation have been
573 found to be ~ 5 m/s and it is believed that this circulation is often a major contributor to convective
574 initiation. The model resolution used in this study is sufficient to at least partially resolve this
575 circulation, thus, in this section composite cross-sections of the near-dryline vertical wind fields are
576 examined in Figure 14, which is constructed similarly to the cross sections in Figs. 10 and 11, except
577 the cross sections are zoomed in on the area from 1.0° west to 1.0° east of the dryline. The composites
578 were constructed for 2011 cases, so that all six available PBL schemes could be compared. The pattern
579 in vertical velocity magnitude is similar for all six PBL members. Maximum upward vertical velocities
580 occur between 850 and 700 hPa and are centered directly over the dryline, while maximum downward
581 vertical velocities occur at or just below 400 hPa and are centered slightly east of the dryline. On
582 average, the strongest vertical velocities occur in the YSU and YSU-T members, with maxima in the
583 composites of 55.9 and 55.3 cm/s, respectively. ACM2 had the smallest maximum vertical velocity at
584 37.1 cm/s, while MYJ, QNSE, and MYNN fell in the middle with 46.1, 46.6, and 42.5 cm/s,
585 respectively. Note, the compositing removes much of the along-dryline variability and the averages are
586 taken over many cases so that strong local maxima are averaged out. However, examining the
587 maximum vertical velocities at various points along the dryline for individual cases, we typically find
588 that the largest upward vertical velocities are in the range 1.5 to 3.0 m/s.

589

590 **4. Summary and discussion**

591 This study examined six versions of the WRF model that were identically configured except for
592 their scheme to parameterize vertical effects of turbulent mixing. The WRF model simulations were
593 run by the Center for Analysis and Prediction of Storms in support of NOAA/Hazardous Weather
594 Testbed Spring Forecasting Experiments conducted during 2010-2012, covered a CONUS domain with
595 4-km grid-spacing, and used the PBL schemes MYJ, MYNN, QNSE, ACM2, YSU, and YSU-T (a

596 version of YSU that was modified in an effort to alleviate its well known warm/dry bias by reducing
597 vertical mixing).

598 Specifically, because of their importance to convective initiation over the southern high plains,
599 as well as their strong dependence on vertical mixing processing in the PBL, this study focuses on 24 h
600 forecast dryline position. Furthermore, the sensitivities of the vertical distribution of thermodynamic
601 and kinematic variables associated with the dryline and near-dryline environment were examined. The
602 main results are summarized below.

603 For two case studies – 12 May 2010 and 24 May 2011 – large eastward errors in 24 h forecast
604 dryline position were found. The magnitude of eastward error was dependent on the PBL scheme and
605 ranged from 0.8° to 2.8° . In both cases, the dryline position errors resulted in large areas being forecast
606 to be outside of the moist sector where there would have been little risk for severe weather, when in
607 reality these areas were within the moist sector where severe weather from dryline-initiated storms
608 occurred. Examining the evolution of the forecast dewpoint from the initialization time in each of the
609 case studies, a dry bias near and to the west of the dryline could be traced back to the NAM initial
610 conditions. Thus, it was suspected that in these cases, the dry bias in the NAM partially contributed to
611 the dryline errors.

612 Examining aggregate statistics on forecast dryline position errors, a statistically significant
613 systematic eastward bias was very apparent. Depending on the set of cases and PBL scheme examined,
614 the mean eastward errors ranged from about 0.5° to 1.25° . Generally, the local schemes MYJ and
615 QNSE had the smallest eastward errors, while the non-local schemes, ACM2 and YSU had the largest
616 eastward errors. However, there were two exceptions to this rule – MYNN, a local scheme, tended to
617 have eastward position errors as large or larger than the non-local schemes, and the YSU-T, a non-local
618 scheme that was only run during 2011, had smaller eastward errors than the local schemes (although its
619 dryline positions were not significantly different than MYJ). Examining the relationship between the

620 bias of the 2-m dewpoint from the initial conditions and the 24 h forecast dryline position found that
621 these two variables were significantly correlated. Thus, it appeared that a systematic dry bias in the
622 NAM analysis at 0000 UTC near and west of the dryline explained much of the eastward position
623 errors. Examining the 24 h forecast dryline positions separately for each year further supported the
624 influence of the NAM dry bias. During 2010 and 2011, dry biases in the NAM over the region -105° W
625 to -99° W and 29° N to 39° N were -2.0°C and -1.25°C , respectively, with corresponding large eastward
626 biases in forecast dryline position. However, during 2012, there was almost no bias (0.02°C) in 2-m
627 dewpoint from the NAM, and the corresponding 24 h dryline position errors in the MYJ and QNSE
628 were near zero, while those in the MYNN were about 0.6° east, which was much less than 2010 and
629 2011, during which MYNN had eastward errors greater than 1.0° . The reduction in the 2-m dewpoint
630 bias of the NAM ICs was likely related to a major upgrade of the NAM model and data assimilation
631 system that occurred in October of 2011. Thus, we believe that dryline position errors in future SSEF
632 system configurations that use the NAM for ICs will have results similar to those of 2012, rather than
633 the earlier years examined.

634 To gain further insight in to how the various PBL scheme depicted the PBL and how they may
635 have been related to the dryline position errors, a procedure was developed to construct dryline-relative
636 composite vertical cross sections of the near-dryline environment for each PBL member. The cross-
637 sections of specific humidity revealed that MYNN, ACM2, and YSU had deeper and drier PBLs than
638 MYJ and QNSE and closely matched results presented in Coniglio et al. (2013). In addition, examining
639 the differences in specific humidity with respect to MYJ, a strong dependence was found on the
640 distance from the dryline. For MYNN, ACM2, and YSU, the largest positive moisture differences
641 relative to MYJ were centered between 850 and 700 hPa and occurred between 1.0° and 3.0° east of the
642 dryline. In the temperature composites, the largest negative temperature differences relative to MYJ in
643 the MYNN, ACM2, and YSU members occurred in the 850 to 700 mb layer about 2.0° to 3.5° east of

644 the dryline which reflected a stronger capping inversion in MYJ relative to the other members. Positive
645 temperature differences existed in the layer adjacent to the ground. The temperature results were
646 consistent with an overall deeper and warmer PBL in the MYNN, ACM2, and YSU members relative to
647 MYJ. The differences in the temperature and moisture cross sections were generally consistent with the
648 differences in forecast dryline position errors – i.e., the tendency to produce warmer/drier/deeper PBLs
649 implies stronger vertical mixing, which results in the dryline mixing farther eastward. Thus, the MYJ
650 and QNSE schemes, which had shallower/moister/cooler PBLs relative to the other schemes also had
651 more westward dryline positions, while the ACM2, MYNN, and YSU schemes, which had
652 deeper/drier/warmer, PBLs had more eastward dryline positions.

653 The composite vertical cross sections of wind magnitude revealed that ACM, MYNN, and YSU
654 generally had stronger wind speeds in the PBL east of the dryline relative to MYJ, which is likely the
655 result of more vertical mixing turbulence in these scheme relative to MYJ. Also, in the QNSE scheme,
656 wind speeds were generally faster than MYJ in the PBL east of the dryline.

657 In comparisons of composite vertical cross sections between YSU and YSU-T, only very small
658 differences in temperature, moisture, and wind were found. This was somewhat surprising given the
659 relatively large differences in forecast dryline position in the YSU and YSU-T members. Further
660 investigation beyond the scope of this study is needed to resolve this apparent discrepancy.

661 To complement the composite vertical cross sections, composite soundings at various distances
662 east and west of the dryline were presented to provide perspective on how sensitive products relevant to
663 severe weather forecasting are to the PBL schemes. The main findings from the composite sounding
664 analyses were that the largest differences between the schemes occurred at 1.0°, 1.5°, 2.0°, and 2.5° east
665 of the dryline. At these distances, CAPE values were much higher in MYJ and QNSE than ACM2,
666 YSU, and MYNN, which was mainly the result of moister low-level dewpoint profiles in these
667 members. Also, at these distances, the temperature profiles in the MYJ and QNSE members were

668 noticeably warmer than YSU, ACM2, and MYNN, reflecting their more pronounced capping
669 inversions. Furthermore, at 1.0° east of the dryline and greater, SRH exhibited more variability, with
670 the faster PBL wind speeds in MYJ, and especially QNSE resulting in more “looped” hodographs and
671 higher SRH than ACM2, MYNN, and YSU. In the comparisons of YSU and YSU-T, the most notable
672 differences were with SRH at 0.5° and 1.0° east of the dryline where stronger low-level winds in YSU
673 resulted in much larger values of SRH.

674 Finally, to examine the depiction of the dryline-induced vertical circulation, composite cross-
675 sections of the near-dryline vertical wind fields were examined for each PBL member. The patterns in
676 vertical velocity among all six PBL members were very similar. Maximum upward velocities occurred
677 between 850 and 700 hPa and were centered directly over the dryline, while maximum downward
678 velocities occurred at or just below 400 hPa and were centered slightly east of the dryline. YSU and
679 YSU-T had the strongest upward velocities, and ACM2 had the smallest.

680 The results of this study illustrate how important it is in convection-allowing modeling
681 applications to consider more than just the depiction of the environmental temperature and moisture.
682 Coniglio et al. (2013) made this point after finding favorable results for MYNN comparing observed
683 versus forecast sounding structures in pre-convective environments and noted, “The fact that MYNN
684 performed best ... does not necessarily mean it will perform the best when evaluated for explicit
685 forecasts of convection or for other characteristics of the simulations that depend on turbulent mixing
686 (e.g., the position of drylines and fronts).” Because current convection-allowing modeling systems like
687 the HRRR utilize MYNN, further work should be conducted to improve its depiction of forecast dryline
688 position. Furthermore, the non-local scheme YSU-T should be examined in more detail because of its
689 superior performance in forecast dryline position.

690

691 **Acknowledgments**

692 Funding was provided by NOAA/Office of Oceanic and Atmospheric Research under NOAA-
693 University of Oklahoma Cooperative Agreement #NA11OAR4320072, U.S. Department of Commerce.
694 CAPS SSEF forecasts were supported by the NOAA Collaborative Science, Technology, and Applied
695 Research (CSTAR) Program with supplementary support from NSF grant AGS-0802888. M. Xue was
696 supported by NSF grants OCI-0905040, AGS-0941491, AGS-1046171, and AGS-1046081. CAPS
697 forecasts were supported by an allocation of advanced computing resources provided by the National
698 Science Foundation. The computations were performed on Athena (a Cray XT4) at the National
699 Institute for Computational Science (<http://www.nics.tennessee.edu/>). CAPS utilized resources from
700 the OU Supercomputing Center for Research and Education for ensemble post-processing. We thank
701 two anonymous reviewers for many helpful comments/suggestions that improved the manuscript.

702

703

704

705

706

707

708

709

710

711

712

713

714

715

716 **References**

- 717 Alexander, C. R., S. S. Weygandt, S. Benjamin, D. C. Dowell, T. G. Smirnova, E. P. James, P.
718 Hofmann, M. Hu, J. M. Brown, and G. A. Grell , 2013: High-Resolution Rapid Refresh (HRRR)
719 Model and Production Advancements for 2013 with Targeted Improvements for Reliable
720 Convective Weather Guidance in the National Airspace System. *Sixteenth Conference on*
721 *Aviation, Range, and Aerospace Meteorology* (ARAM), Austin, TX.
- 722 Atkins, N. T., R. M. Wakimoto, and C. L. Ziegler, 1998: Observations of the finescale structure of a
723 dryline during VORTEX 95. *Mon. Wea. Rev.*, **126**, 525–550.
- 724 Baldwin, M. E., and K. E. Mitchell, 1997: The NCEP hourly multisensory U.S. precipitation analysis
725 for operations and GCIP research. Preprints, *13th Conf. on Hydrology*, Long Beach, CA, Amer.
726 Meteor. Soc., 54-55.
- 727 Benjamin, S. G., and Coauthors, 2004a: An hourly assimilation–forecast cycle: The RUC. *Mon. Wea.*
728 *Rev.*, **132**, 495–518.
- 729 Benjamin, S. G., G. A. Grell, J. M. Brown, T. G. Smirnova, and R. Bleck, 2004b: Mesoscale weather
730 prediction with the RUC hybrid isentropic–terrain-following coordinate model. *Mon. Wea. Rev.*,
731 **132**, 473–494.
- 732 Brown, J., and Coauthors, 2012: Rapid Refresh replaces the Rapid Update Cycle at NCEP. 2012
733 *Canadian Meteorological and Oceanographic Society Congress/21st Numerical Weather*
734 *Prediction Conference/25th Weather and Forecasting Conference*, Montreal, Canada, 3B1.
- 735 Chen, F., and J. Dudhia, 2001: Coupling an advanced land-surface/ hydrology model with the Penn
736 State/ NCAR MM5 modeling system. Part I: Model description and implementation. *Mon. Wea.*
737 *Rev.*, **129**, 569–585.
- 738 Chou M.-D., and M. J. Suarez, 1994: An efficient thermal infrared radiation parameterization for use in
739 general circulation models. NASA Tech. Memo. 104606, 3, 85pp.

740 Clark, A. J., and Coauthors, 2012a: An overview of the 2010 Hazardous Weather Testbed Experimental
741 Forecast Program Spring Experiment. *Bull. Amer. Meteor. Soc.*, **93**, 55-74.

742 Coffey, B. E., L. C. Maudlin, P. G. Veals, and A. J. Clark, 2013: Dryline position errors in experimental
743 convection-allowing NSSL-WRF model forecasts and the operational NAM. *Wea. Forecasting*,
744 **28**, 746–761.

745 Coniglio, M. C., J. Correia, P. T. Marsh, and F. Kong, 2013: Verification of convection-allowing WRF
746 model forecasts of the planetary boundary layer using sounding observations. *Wea. Forecasting*,
747 **28**, 842–862.

748 Coniglio, M. C., 2012: Verification of RUC 0–1-h Forecasts and SPC Mesoscale Analyses Using
749 VORTEX2 Soundings. *Wea. Forecasting*, **27**, 667–683.

750 Davies-Jones, R., D. Burgess, and M. Foster, 1990: Test of helicity as a tornado forecast
751 parameter. Preprints, *16th Conf. on Severe Local Storms* Kananaskis Park, AB, Canada, Amer.
752 Meteor. Soc., 588–592.

753 Du, J., J. McQueen, G. DiMego, Z. Toth, D. Jovic, B. Zhou, and H.-Y. Chuang, 2006: New dimension
754 of NCEP Short-Range Ensemble Forecasting (SREF) system: Inclusion of WRF members. *WMO*
755 *Expert Team Meeting on Ensemble Prediction Systems*, Exeter, United Kingdom, WMO, 5 pp.
756 [Available online at http://www.emc.ncep.noaa.gov/mmb/SREF/WMO06_full.pdf.]

757 Fujita, T. T., 1958: Structure and movement of a dry front. *Bull. Amer. Meteor. Soc.*, **39**, 574–582.

758 Gao, J., M. Xue, K. Brewster, and K. K. Droegemeier, 2004: A three-dimensional variational data
759 analysis method with recursive filter for Doppler radars. *J. Atmos. Ocean. Tech.*, **21**, 457-469.

760 Hane, C. E., H. B. Bluestein, T. M. Crawford, M. E. Baldwin, and R. M. Rabin, 1997: Severe
761 thunderstorm development in relation to along-dryline variability: A case study. *Mon. Wea. Rev.*,
762 **125**, 231–251.

763 Hu, M., M. Xue, and K. Brewster, 2006: 3DVAR and cloud analysis with WSR-88D level-II data for

764 the prediction of Fort Worth tornadic thunderstorms. Part I: Cloud analysis and its impact. *Mon.*
765 *Wea. Rev.*, **134**, 675-698.

766 Hu, X.-M., J. W. Nielsen-Gammon, and F. Zhang, 2010: Evaluation of three planetary boundary layer
767 schemes in the WRF model. *J. Appl. Meteor. Climatol.*, **49**, 1831–1843.

768 Janjic, Z. I., 2002: Nonsingular implementation of the Mellor-Yamada Level 2.5 Scheme in the NCEP
769 Meso model. NCEP Office Note No. 437, NOAA/NWS, 61 pp.

770 Kong, F., and Coauthors, 2010: Evaluation of CAPS multi-model storm-scale ensemble forecast for the
771 NOAA HWT 2010 Spring Experiment. *25th Conf. Severe Local Storms*, Amer. Meteor. Soc.,
772 Paper P4.18.

773 Kong, F., and Coauthors, 2011: CAPS storm-scale ensemble forecast in HWT 2011 Spring Experiment:
774 Sensitivity of WRF physics on QPF. *Extended Abstracts, 12th Users' Workshop*, Boulder, CO,
775 NCAR. [Available online at
776 [http://www.mmm.ucar.edu/wrf/users/workshops/WS2011/Power%20Points%202011/6_3_Kong_](http://www.mmm.ucar.edu/wrf/users/workshops/WS2011/Power%20Points%202011/6_3_Kong_WRFworkshop_11.pdf)
777 [WRFworkshop_11.pdf](http://www.mmm.ucar.edu/wrf/users/workshops/WS2011/Power%20Points%202011/6_3_Kong_WRFworkshop_11.pdf).]

778 Marshall, C. H., K. C. Crawford, K. E. Mitchell, and D. J. Stensrud, 2003: The impact of the land
779 surface physics in the operational NCEP Eta Model on simulating the diurnal cycle: Evaluation
780 and testing using Oklahoma Mesonet data. *Wea. Forecasting*, **18**, 748–768.

781 Mellor, G. L., and T. Yamada, 1982: Development of a turbulence closure model for geophysical fluid
782 problems. *Rev. Geophys.*, **20**, 851–875.

783 Miller, P. A., M. F. Barth, and L. A. Benjamin, 2005: An update on MADIS observation ingest,
784 integration, quality control and distribution capabilities. Preprints, *21st Int. Conf. on Interactive*
785 *Information and Processing Systems*, San Diego, CA, Amer. Meteor. Soc., J7.12. [Available
786 online at <https://ams.confex.com/ams/pdfpapers/86703.pdf>.]

787 —, —, —, R. S. Artz, and W. R. Pendergrass, 2007: MADIS support for UrbaNet. Preprints,

788 *14th Symp. on Meteorological Observation and Instrumentation/16th Conf. on Applied*
789 *Climatology*, San Antonio, TX, Amer. Meteor. Soc., JP2.5. [Available online at
790 <http://ams.confex.com/ams/pdfpapers/119116.pdf>.]

791 Mlawer, E. J., S. J. Taubman, P. D. Brown, M. J. Iacono, and S. A. Clough, 1997: Radiative transfer for
792 inhomogeneous atmosphere: RRTM, a validated correlated-k model for the long-wave. *J.*
793 *Geophys. Res.*, 102(D14), 16663-16682.

794 Nakanishi, M., 2000: Large-eddy simulation of radiation fog. *Bound.-Layer Meteor.*, **94**, 461–493.
795 ———, 2001: Improvement of the Mellor–Yamada turbulence closure model based on large-eddy
796 simulation data. *Bound.-Layer Meteor.*, **99**, 349–378.

——— and H. Niino, 2004: An improved Mellor–Yamada level-3 model with condensation physics: Its
design and verification. *Bound.-Layer Meteor.*, **112**, 1–31.

797 ———, and ———, 2006: An improved Mellor–Yamada level-3 model: Its numerical stability and
798 application to a regional prediction of advection fog. *Bound.-Layer Meteor.*, **119**, 397–407.

799 Noh, Y., W. G. Cheon, S.-Y. Hong, and S. Raasch, 2003: Improvement of the K-profile model for the
800 planetary boundary layer based on large eddy simulation data. *Bound.-Layer Meteor.*, **107**, 401–
801 427.

802 Parsons, D. B., M. A. Shapiro, R. M. Hardesty, R. J. Zamora, and J. M. Intrieri, 1991: The finescale
803 structure of a West Texas dryline. *Mon. Wea. Rev.*, **119**, 1242–1258.

804 Pleim, J. E., 2007: A combined local and nonlocal closure model for the atmospheric boundary layer.
805 Part I: Model description and testing. *J. Appl. Meteor. Climatol.*, **46**, 1383–1395.

806 R Development Core Team, cited 2013: R: A language and environment for statistical computing. R
807 Foundation for Statistical Computing, Vienna, Austria. [Available online at [http://www.R-](http://www.R-project.org)
808 [project.org](http://www.R-project.org).]

809 Rhea, J. O., 1966: A study of thunderstorm formation along dry lines. *J. Appl. Meteor.*, **5**, 59–63.

- 810 Roebber, P. J., D. M. Schultz, B. A. Colle, D. J. Stensrud, 2004: Toward improved prediction: High-
811 resolution and ensemble modeling systems in operations. *Wea. Forecasting*, **19**, 936–949.
- 812 Rogers, E., and Coauthors, 2009: The NCEP North American Mesoscale modeling system: Recent
813 changes and future plans. *Preprints, 23rd Conference on Weather Analysis and Forecasting/19th*
814 *Conference on Numerical Weather Prediction*, Omaha, NE, Amer. Meteor. Soc., 2A.4.
- 815 Schaefer, J. T., 1986: The dryline. *Mesoscale Meteorology and Forecasting*, P. S. Ray, Ed., Amer.
816 Meteor. Soc., 549–572.
- 817 Skamarock, W. C., and Coauthors, 2008: A description of the Advanced Research WRF Version 2,
818 NCAR Tech Note, NCAR/TN-475+STR, 113 pp. [Available at:
819 http://www.mmm.ucar.edu/wrf/users/docs/arw_v3.pdf.]
- 820 Sukoriansky, S., B. Galperian, and V. Perov, 2005: Application of a new spectral theory of stable
821 stratified turbulence to the atmospheric boundary layer over sea ice. *Bound.-Layer Meteor.*, **117**,
822 231–257.
- 823 Thompson, G., R. M. Rasmussen, and K. Manning, 2004: Explicit forecasts of winter precipitation
824 using an improved bulk microphysics scheme. Part I: Description and sensitivity analysis. *Mon.*
825 *Wea. Rev.*, **132**, 519–542.
- 826 Xue, M., D. Wang, J. Gao, K. Brewster, and K. K. Droegemeier, 2003: The Advanced Regional
827 Prediction System (ARPS), storm-scale numerical weather prediction and data assimilation.
828 *Meteor. Atmos. Phys.*, **82**, 139-170.
- 829 ———, and Coauthors, 2008: CAPS realtime storm-scale ensemble and high-resolution forecasts as part
830 of the NOAA Hazardous Weather Testbed 2008 Spring Experiment. *24th Conf. Severe Local*
831 *Storms*, Savannah, GA, Amer. Meteor. Soc., 12.2.
- 832 ———, and Coauthors, 2010: CAPS realtime storm scale ensemble and high-resolution forecasts for the
833 NOAA Hazardous Weather Testbed 2010 Spring Experiment. *25th Conf. On Severe Local Storms*,

834 Denver, CO, Amer. Meteor. Soc., 7B.3.

835 Ziegler, C. L., and C. E. Hane, 1993: An Observational Study of the Dryline. *Mon. Wea. Rev.*, **121**,
836 1134–1151.

837 ———, W. J. Martin, R. A. Pielke, and R. L. Walko, 1995: A modeling study of the dryline. *J. Atmos.*
838 *Sci.*, **52**, 263–285.

839 ———, and E. N. Rasmussen, 1998: The initiation of moist convection at the dryline: Forecasting issues
840 from a case study perspective. *Wea. Forecasting*, **13**, 1106–1131.

841

842

843

844

845

846

847

848

849

850

851

852

853

854

855

856

857

858 **List of Tables**

859 Table 1 A summary of code changes and their intended effects in the modified version of YSU provided
860 by Greg Thompson (YSU-T).

861 Table 2 Model specifications for SSEF members with different boundary layer parameterizations.
862 WRF model versions were 3.1.1, 3.2.1, and 3.3.1 for the years 2010, 2011, and 2012,
863 respectively. Boundary layer schemes include MYJ (Mellor and Yamada 1982; Janjic 2002),
864 MYNN (Nakanishi 2000, 2001; Nakanishi and Niino 2004, 2006), QNSE (Sukoriansky et al.
865 2006), YSU (Noh et al. 2003), ACM2 (Pleim 2007), and YSU-Thompson (modified version of
866 YSU described in text). All simulations used Thompson et al. (2004) microphysics, Rapid
867 Radiative Transfer Model (RRTM; Mlawer et al. 1997) shortwave radiation and Goddard (Chou
868 and Suarez 1994) longwave radiation parameterizations, and the Noah (Chen and Dudhia 2001)
869 land surface models. ARPSa refers to ARPS 3DVAR and cloud analysis, which uses NAM
870 analyses as the background. NAMf refers to NAM forecasts (12-km grid-spacing).

871

872

873

874

875

876

877

878

879

880

881

882 **List of Figures**

883 Figure 1 Dewpoint (shaded; F) valid 0000 UTC 13 May 2010 with manually defined dryline locations
884 denoted by grey lines for 24 h forecasts from (a) MYJ, (b) MYNN, (c) QNSE, and (d) the RUC
885 analysis. (e) Dryline locations for (a) – (d) are shown together (colored lines) along with all the
886 other non-PBL SSEF system members (grey lines; legend provided in lower right). The green
887 shaded region indicates a “slight risk” for severe weather as determined by SPC as part of their
888 severe weather outlook issued at 2000 UTC 12 May 2010. Locations of severe storm reports that
889 occurred within a 6 h window centered at 0000 UTC 13 May are marked (legend in upper left).
890 The black horizontal line at 34 degrees N latitude denotes the area used in the panel (f) time-
891 longitude section. (f) Time-longitude plot of forecast and observed dryline locations at 34 degrees
892 N latitude from 0000 UTC 12 May to 0000 UTC 13 May.

893 Figure 2 Dewpoint (shaded; F) valid 0000 UTC 12 May 2010 (forecast hour 0) from the (a) RUC
894 analysis, (b) MYJ without 3DVAR data assimilation, and (c) MYJ with 3DVAR data assimilation.
895 (d) Dewpoint difference between MYJ without 3DVAR data assimilation and the RUC analysis,
896 and (e) dewpoint difference between MYJ with 3DVAR data assimilation and MYJ without
897 3DVAR data assimilation. (f) – (j), (k) – (o), (p) – (t), (u) – (y), and (z) – (δ), same as (a) – (e)
898 except valid at forecast hours 3, 6, 12, 18, and 24, respectively.

899 Figure 3 Dewpoint (C; shaded) and 10-m wind barbs (knots) valid 0000 UTC 12 May 2010 from
900 analyses of the (a) RUC and (b) NAM. The different colored and sized dots depict locations of
901 observations valid near the corresponding time and contained in the Meteorological Assimilation
902 Data Ingest System (MADIS) dataset. Larger dot sizes indicate larger differences between the
903 MADIS observations and nearest analysis grid-point, with the brown (green) shades indicating the
904 analysis is dry (moist) relative to the MADIS observations. A legend for the dots is provided at
905 the top of each panel.

906 Figure 4 Dewpoint (shaded; F) valid 0000 UTC 25 May 2011 with manually defined dryline locations
907 denoted by grey lines for 24 h forecasts from (a) MYJ, (b) MYNN, (c) QNSE, (d) ACM2, (e)
908 YSU, (f) YSU-T, and (g) the RUC analysis. (h) Dryline locations for (a) – (g) are shown together
909 (colored lines) along with all the other non-PBL SSEF system members (grey lines; legend
910 provided on left side). The green, red, and purple shaded region indicate “slight”, “moderate”,
911 and “high” risks for severe weather as determined by SPC as part of their severe weather outlook
912 issued at 2000 UTC 24 May 2011. Locations of severe storm reports that occurred within a 6 h
913 window centered at 0000 UTC 25 May are marked (legend in lower right). The black horizontal
914 line at 34 degrees N latitude denotes the area used in the panel (i) time-longitude section. (i)
915 Time-longitude plot of forecast and observed dryline locations at 34 degrees N latitude from 0000
916 UTC 24-25 May 2011.

917 Figure 5 Dewpoint (shaded; F) valid 0000 UTC 24 May 2011 (forecast hour 0) from the (a) RUC
918 analysis, (b) MYJ without 3DVAR data assimilation, and (c) MYJ with 3DVAR data assimilation.
919 (d) Dewpoint difference between MYJ without 3DVAR data assimilation and the RUC analysis,
920 and (e) dewpoint difference between MYJ with 3DVAR data assimilation and MYJ without
921 3DVAR data assimilation. (f) – (j), (k) – (o), (p) – (t), and (u) – (y), same as (a) – (e) except valid
922 at forecast hours 3, 6, 12, and 18 respectively.

923 Figure 6 Box plots for the distribution of average longitudinal dryline position errors for the sets of
924 cases covering 2010-2012, 2011-2012, and 2011-only (left side). The right side box plots are for
925 the differences in dryline position with respect to MYJ. The interquartile range (IQR) within each
926 box plot is colored according to the particular boundary layer scheme (indicated on y-axis). The
927 under-laid pink shading indicates that differences with respect to the observations (left side) or
928 MYJ (right side) were statistically significant at $\alpha = 0.05$. The median is indicated by the straight
929 black line through each box, the box encompasses the IQR, outliers defined by values outside of

930 1.5 x IQR are marked by crosses, and horizontal lines (whiskers) denote the smallest and largest
931 values that are not outliers. The map of Oklahoma is shown for reference – its horizontal scale
932 matches that of the x-axis for the box plots.

933 Figure 7 Scatterplots of average 2-m dewpoint bias in the NAM initial conditions for the area bounded
934 by -105 to -99 degrees west longitude and 29 to 39 degrees north latitude versus average
935 longitudinal dryline error for (a) MYJ, (b) QNSE, and (c) MYNN. The red lines show the “best
936 fit” computed using linear regression. Correlation coefficients (R) are shown at the bottom left
937 along with the corresponding p-values. (d) Overlay of best fit lines from (a), (b), and (c).

938 Figure 8 (a) On the left, mean 2-m dewpoint errors in the NAM ICs for the 2010 dryline cases. On the
939 right, box plots for the distribution of average longitudinal dryline position errors for the 2010
940 cases. The box plots are constructed similarly to those in Figure 6. (b) and (c) same as (a) except
941 for the years 2011 and 2012, respectively.

942 Figure 9 (a) Specific humidity (shaded; kg/kg) at the lowest model level in the 24 h forecast from the
943 MYJ member valid 0000 UC 11 May 2010. The area enclosed by the thick black line is the area
944 over which a composite dryline cross-section was constructed. The thin black line inside of this
945 area marks the dryline. The horizontal gray dashed lines within the area that are marked (b), (c),
946 and (d) show the location of individual vertical cross sections of specific humidity (shaded) and
947 pressure (red contours) in panels (b), (c), and (d). (e) Composite vertical cross section of specific
948 humidity and pressure constructed by taking the average of cross sections anchored every 0.15
949 degrees latitude along the dryline. (f) – (j) same as (a) – (e), except for the MYNN member.

950 Figure 10 Composite vertical cross sections of specific humidity (shaded; g/kg), pressure (red contours;
951 mb) and upward vertical velocity (black contours at 1 Pa s^{-1} increments from -1 to -6 Pa s^{-1}) over
952 all 2011-2012 cases for (a) MYJ, (b) QNSE, (c) MYNN, (d) ACM2, (e) YSU. Pressure (red
953 contours) and specific humidity difference relative to MYJ (shaded) for (f) QNSE, (g) MYNN,

954 (h) ACM2, and (i) YSU. (j) – (r) and (s) – (α) same as (a) – (i) except for temperature and wind
955 magnitude, respectively.

956 Figure 11 Composite vertical cross sections of specific humidity (shaded; g/kg), pressure (red contours;
957 mb) and upward vertical velocity (black contours) over all 2011 cases for (a) MYJ, (b) YSU, and
958 (c) YSU-T. Pressure (red contours) and specific humidity difference relative to MYJ (shaded)
959 for (d) YSU and (e) YSU-T. (f) Specific humidity difference between YSU and YSU-T. (g) – (l)
960 and (m) – (r) same as (a) – (f) except for temperature and wind magnitude, respectively.

961 Figure 12 Dryline-relative composite soundings and hodographs over the lowest 800 mb of each profile
962 from MYJ, QNSE, MYNN, YSU, and ACM2 for the 2011-2012 (30 cases). Solid lines depict the
963 temperature and dewpoint traces, and the dashed lines trace the path of surface-based air parcels.
964 The north-south “anchor point” of the composite soundings was found by following the dryline 1
965 degree south from its northernmost point. Then, the composites were constructed by taking
966 averages over all cases at the following distances relative to the dryline anchor point: (a) 1.0
967 degrees west, (b) 0.5 degrees east, (c) 1.0 degrees east, (d) 1.5 degrees east, (e) 2.0 degrees east,
968 and (f) 2.5 degrees east. CAPE, CIN, and Storm-relative helicity over the bottom 100 and 300
969 mb layers (SRH1 and SRH3, respectively) are shown for each member at the top-right of each
970 panel. The text color of each member corresponds to the color of each member’s temperature
971 and dewpoint trace. In the hodographs the storm motion vector is shown, which was computed
972 following Davies-Jones et al. (1990).

973 Figure 13 Same as Figure 12, expect profiles are from YSU and YSUT for the 2011 drylines (14 cases).

974 Figure 14 Dryline-relative composite vertical velocity magnitude (shaded; m/s) for 2011 (14 cases).
975 Wind vectors depict the u and w components with the w-component multiplied by a factor of 50
976 to emphasize the vertical component. Pressure (hPa) is shown by the dark red contours. The 7
977 kg/kg specific humidity contour (green) is shown to delineate the moist sector. The maximum

978 vertical velocity in each cross section is provided at the top of each panel. Each panel displays a
979 different PBL member: (a) MYJ, (b) QNSE, (c) MYNN, (d) ACM2, (e) YSU, and (f) YSU-T.

980
981
982
983
984
985
986
987
988
989
990
991
992
993
994
995
996
997
998
999
1000
1001
1002
1003
1004
1005
1006
1007
1008
1009
1010
1011
1012
1013
1014
1015
1016
1017
1018
1019
1020
1021
1022
1023

1024
1025
1026

Table 1 A summary of code changes and their intended effects in the modified version of YSU provided by Greg Thompson (YSU-T).

Description of code change	Intended effect
Surface-based convective perturbation velocity set to zero.	Lower the diagnosed PBL height.
When calculating the wind shear squared term in the Bulk Richardson number (Ri), do not assume zero wind at lower boundary but rather 25% of lowest model level wind.	Reduce downward momentum flux due to large denominator in Ri from higher wind speeds close to surface.
Calculate the thermodynamic term of Ri using $\partial\theta_{IL} / \partial z$ not $\partial\theta_v / \partial z$, where θ_{IL} is ice-liquid water potential temperature and θ_v is virtual potential temperature.	Treat cloud-topped boundary layers as entirely connected within the PBL; otherwise, cloud-topped PBLs result in the cloud layer being split as a fraction within and a fraction above the PBL giving inconsistent profiles of final mixing coefficients.
Disable the explicit entrainment factor at top of PBL.	Mitigate perceived bias of excessive loss of water vapor from PBL and into free troposphere above.
Compute local Ri -based mixing coefficients as done for layers above PBL top and assign final value as the maximum of local and non-local values.	As an offset to disabling explicit entrainment at top of PBL, well-mixed PBLs topped with clouds will have higher entrainment at cloud top than without this modification.

1027
1028
1029
1030
1031
1032
1033
1034
1035
1036
1037
1038
1039
1040
1041
1042
1043
1044
1045
1046
1047
1048
1049
1050
1051
1052
1053
1054
1055
1056
1057
1058
1059
1060

1061 Table 2 Model specifications for SSEF members with different PBL schemes. All simulations used
 1062 Thompson et al. (2004) microphysics, Rapid Radiative Transfer Model (RRTM; Mlawer et al.
 1063 1997) shortwave radiation and Goddard (Chou and Suarez 1994) longwave radiation
 1064 parameterizations, and the Noah (Chen and Dudhia 2001) land surface models. ARPSa refers to
 1065 ARPS 3DVAR and cloud analysis, which uses NAM analyses as the background. NAMf refers to
 1066 NAM forecasts (12-km grid-spacing).
 1067

Boundary Layer Scheme		Years available	# of cases		
MYJ		2010-2012	40		
MYNN		2010-2012	40		
QNSE		2010-2012	40		
ACM2		2011-2012	30		
YSU		2011-2012	30		
YSU-T		2011	14		
Other model specifications (valid for all simulations)					
Microphysics	Shortwave radiation scheme	Longwave radiation scheme	Initial conditions	Lateral boundary conditions	Land surface model
Thompson	Goddard	RRTM	0000 UTC ARPSa	0000 UTC NAMf	Noah

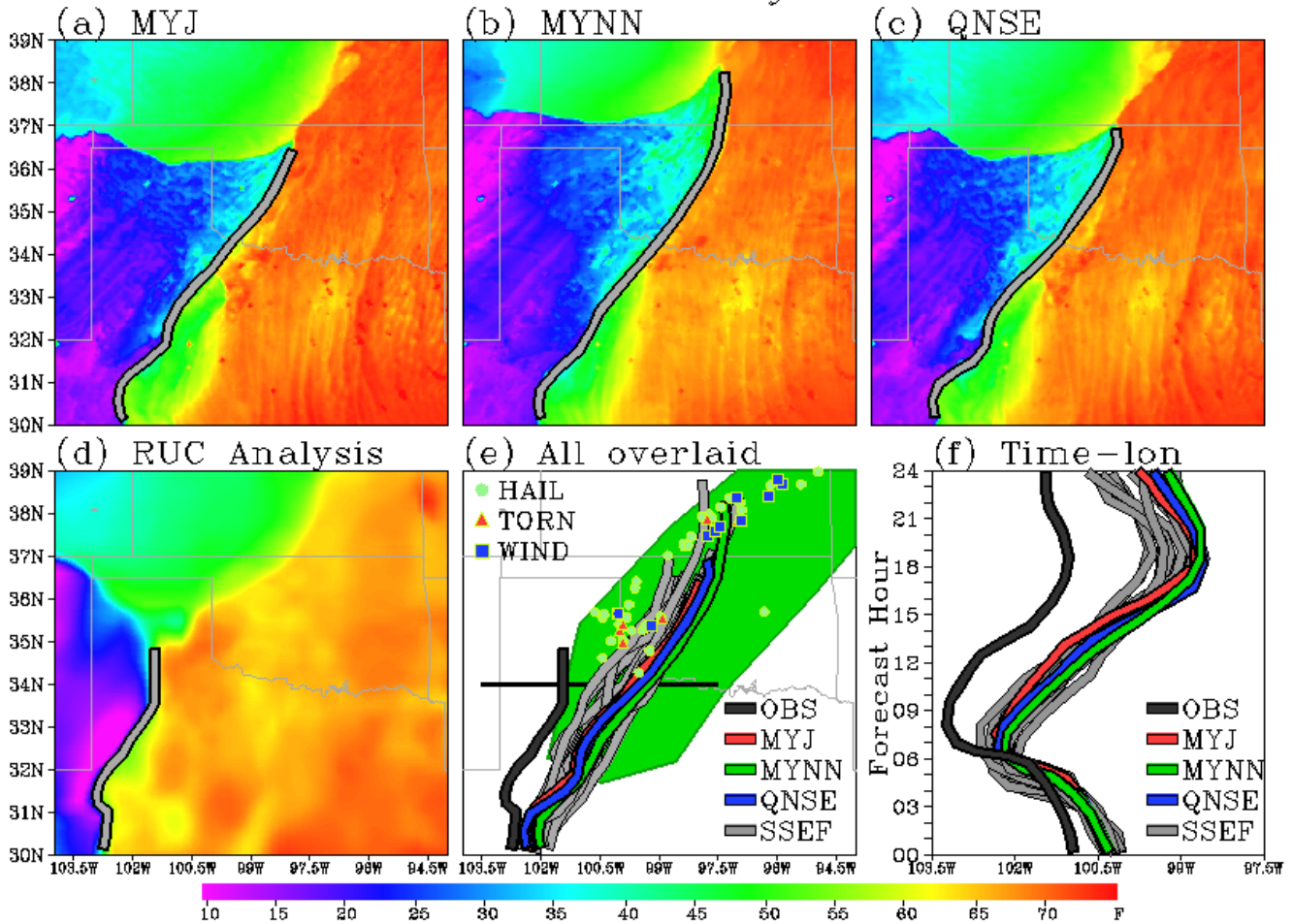
1068

1069

1070

1071

0000 UTC 13 May 2010



1072
1073
1074
1075
1076
1077
1078
1079
1080
1081
1082
1083
1084
1085
1086

Figure 1 Dewpoint (shaded; F) valid 0000 UTC 13 May 2010 with manually defined dryline locations denoted by grey lines for 24 h forecasts from (a) MYJ, (b) MYNN, (c) QNSE, and (d) the RUC analysis. (e) Dryline locations for (a) – (d) are shown together (colored lines) along with all the other non-PBL SSEF system members (grey lines; legend provided in lower right). The green shaded region indicates a “slight risk” for severe weather as determined by SPC as part of their severe weather outlook issued at 2000 UTC 12 May 2010. Locations of severe storm reports that occurred within a 6 h window centered at 0000 UTC 13 May are marked (legend in upper left). The black horizontal line at 34 degrees N latitude denotes the area used in the panel (f) time-longitude section. (f) Time-longitude plot of forecast and observed dryline locations at 34 degrees N latitude from 0000 UTC 12 May to 0000 UTC 13 May.

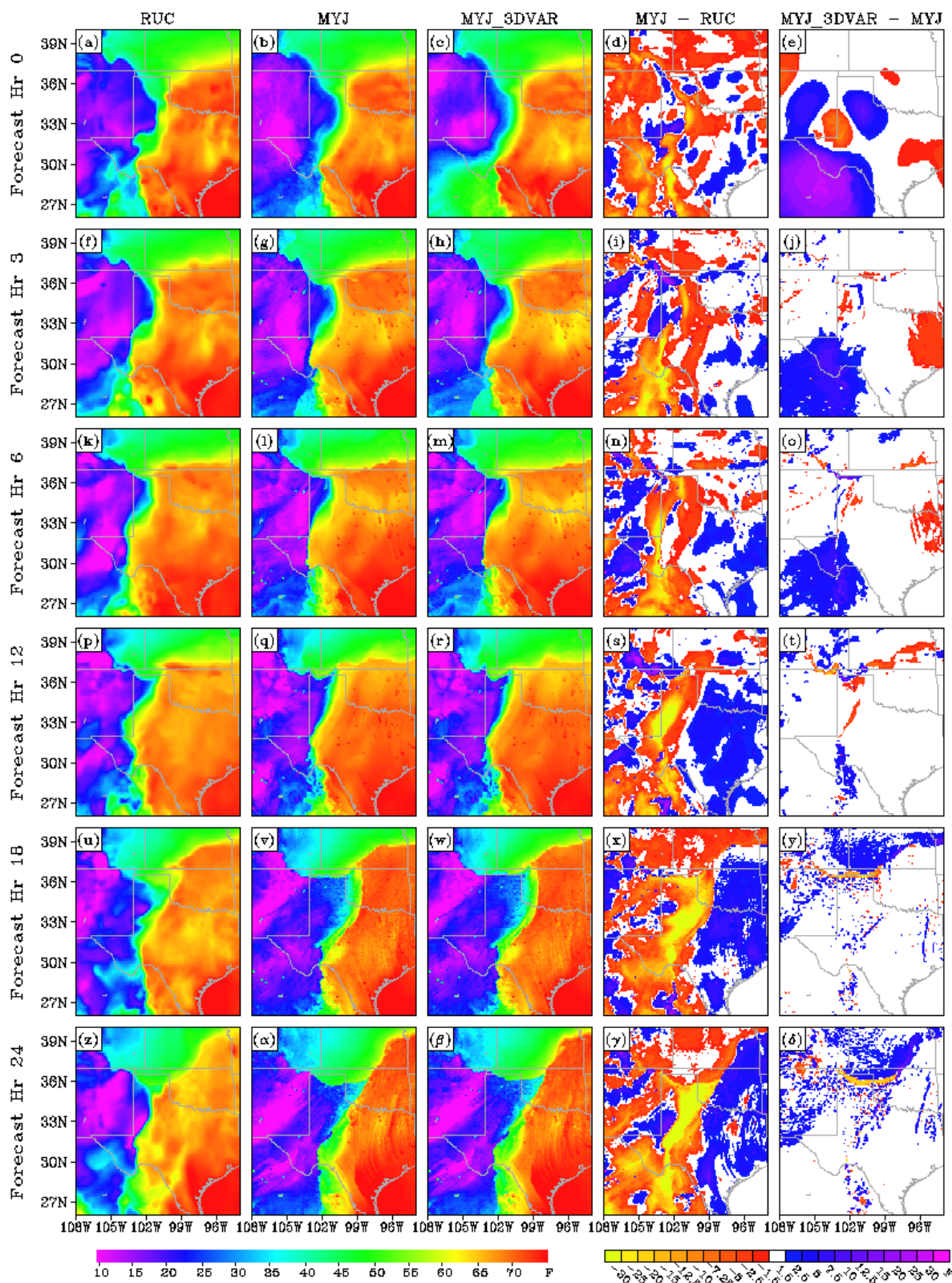
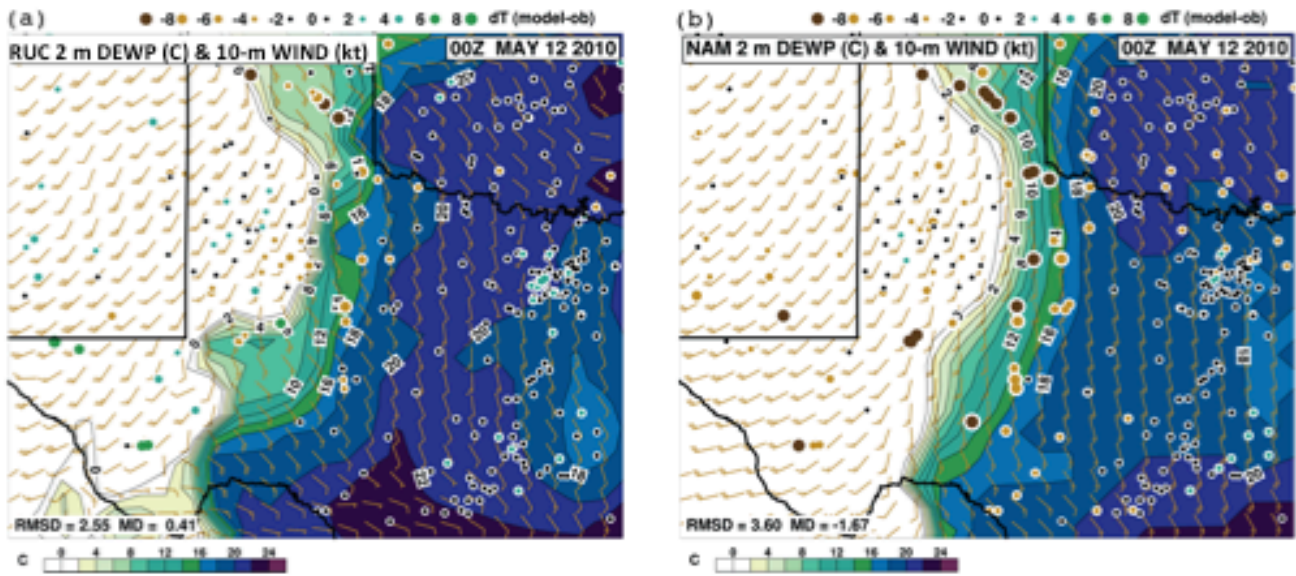


Figure 2 Dewpoint (shaded; F) valid 0000 UTC 12 May 2010 (forecast hour 0) from the (a) RUC analysis, (b) MYJ without 3DVAR data assimilation, and (c) MYJ with 3DVAR data assimilation. (d) Dewpoint difference between MYJ without 3DVAR data assimilation and the RUC analysis, and (e) dewpoint difference between MYJ with 3DVAR data assimilation and MYJ without 3DVAR data assimilation. (f) – (j), (k) – (o), (p) – (t), (u) – (y), and (z) – (δ), same as (a) – (e) except valid at forecast hours 3, 6, 12, 18, and 24, respectively.

1087
1088
1089
1090
1091
1092
1093



1094
 1095
 1096
 1097
 1098
 1099
 1100
 1101
 1102
 1103
 1104
 1105
 1106
 1107
 1108
 1109
 1110
 1111

Figure 3 Dewpoint (C; shaded) and 10-m wind barbs (knots) valid 0000 UTC 12 May 2010 from analyses of the (a) RUC and (b) NAM. The different colored and sized dots depict locations of observations valid near the corresponding time and contained in the Meteorological Assimilation Data Ingest System (MADIS) dataset. Larger dot sizes indicate larger differences between the MADIS observations and nearest analysis grid-point, with the brown (green) shades indicating the analysis is dry (moist) relative to the MADIS observations. A legend for the dots is provided at the top of each panel.

0000 UTC 25 May 2011

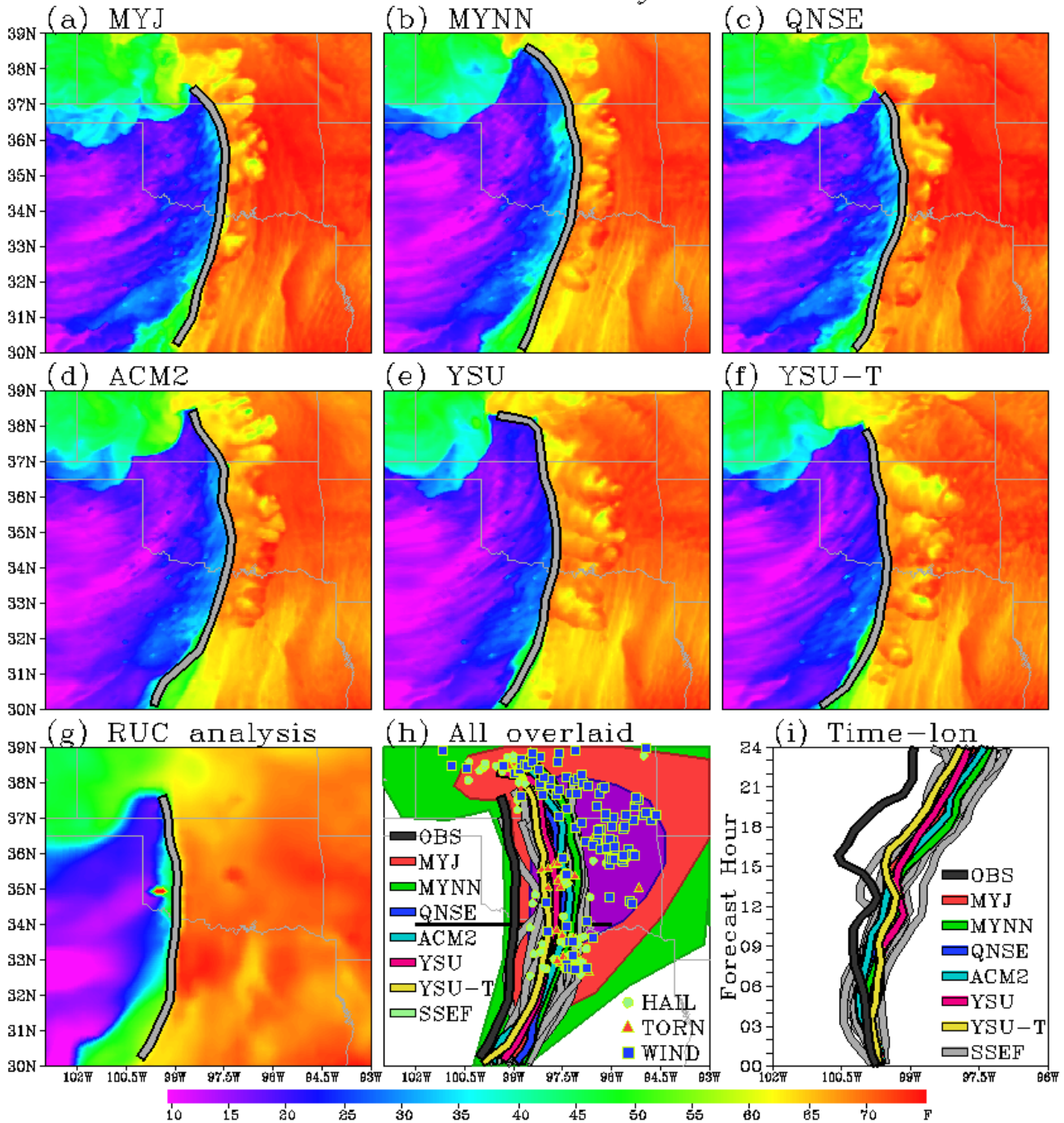
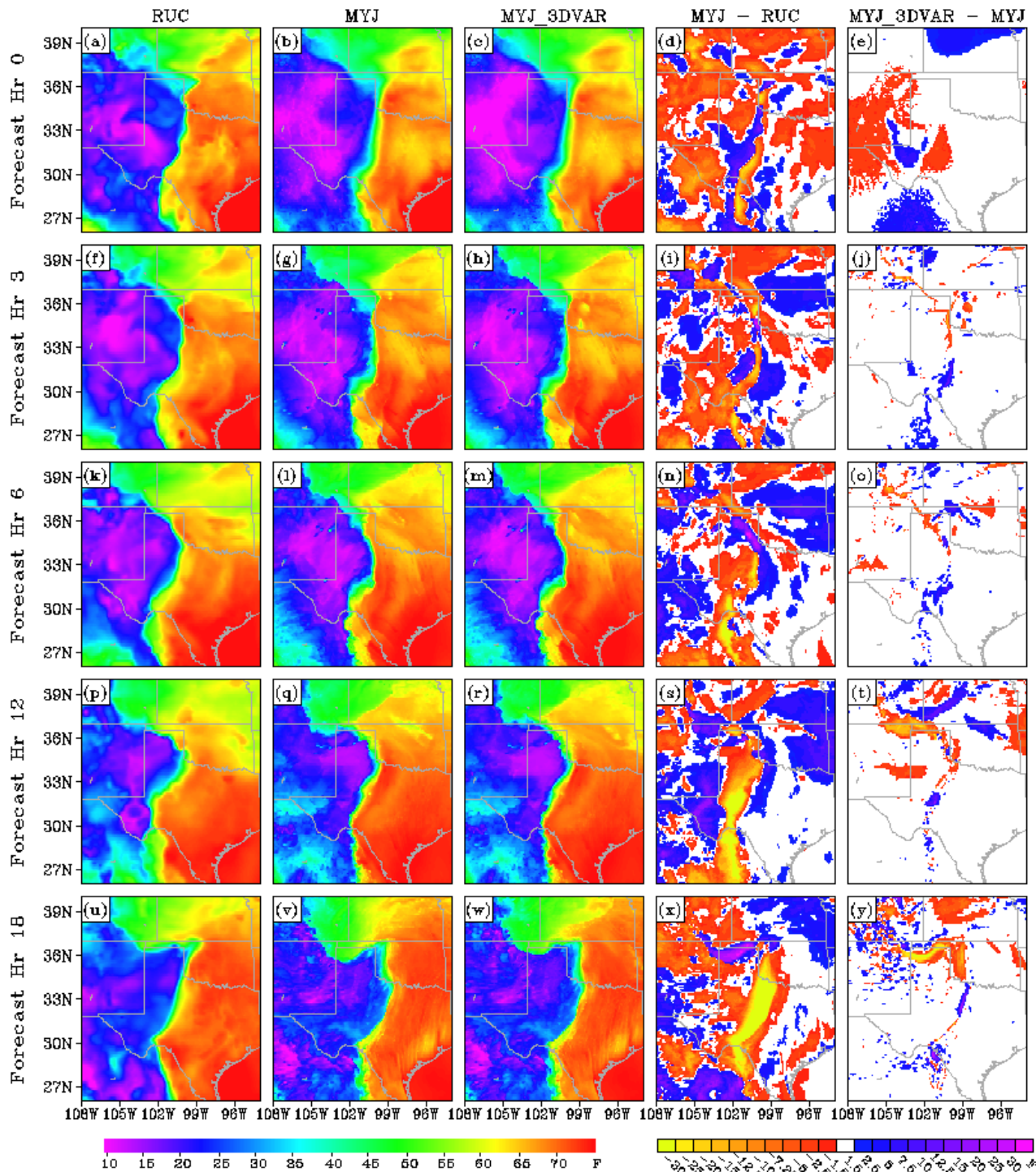
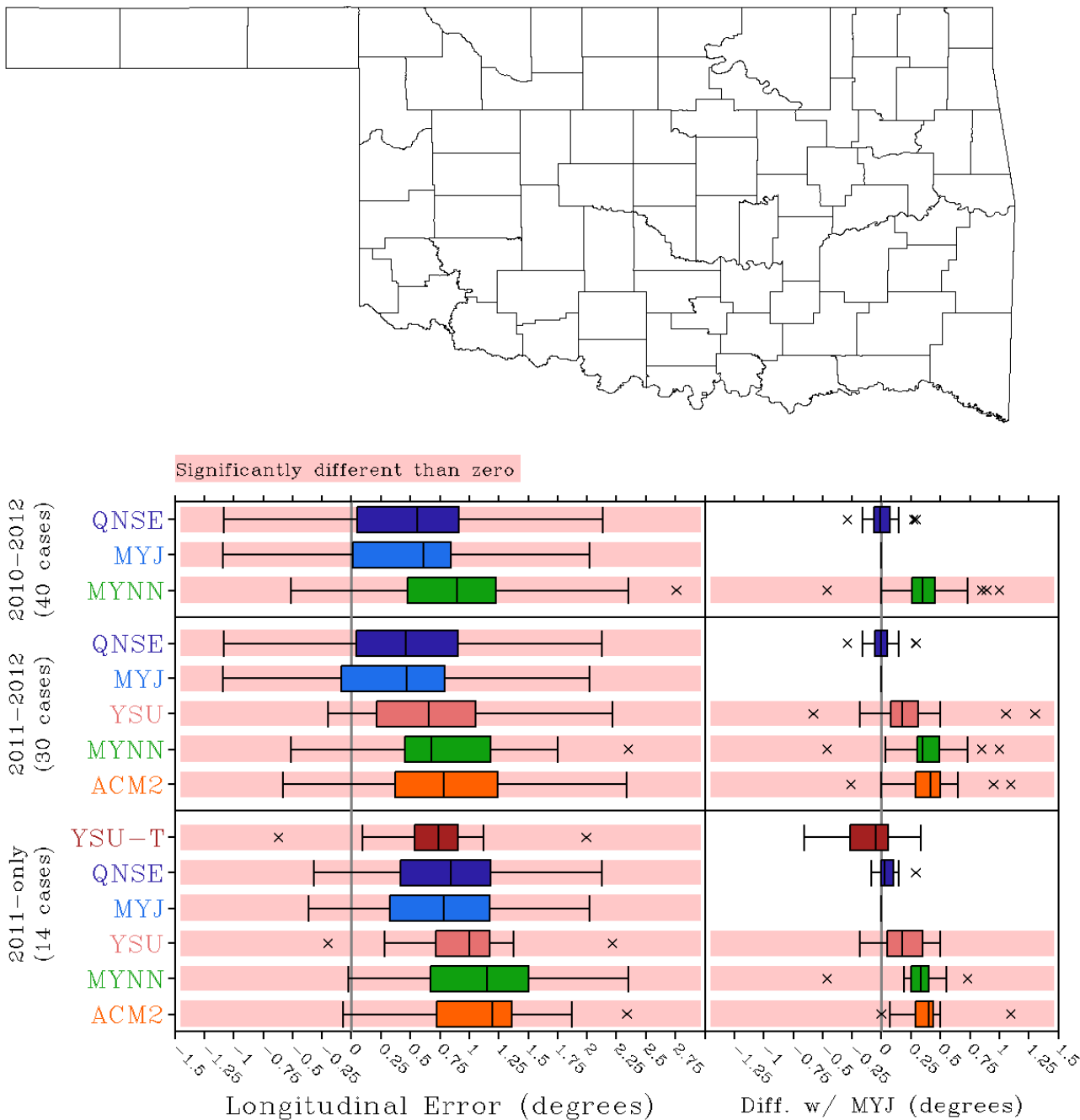


Figure 4 Dewpoint (shaded; F) valid 0000 UTC 25 May 2011 with manually defined dryline locations denoted by grey lines for 24 h forecasts from (a) MYJ, (b) MYNN, (c) QNSE, (d) ACM2, (e) YSU, (f) YSU-T, and (g) the RUC analysis. (h) Dryline locations for (a) – (g) are shown together (colored lines) along with all the other non-PBL SSEF system members (grey lines; legend provided on left side). The green, red, and purple shaded region indicate “slight”, “moderate”, and “high” risks for severe weather as determined by SPC as part of their severe weather outlook issued at 2000 UTC 24 May 2011. Locations of severe storm reports that occurred within a 6 h window centered at 0000 UTC 25 May are marked (legend in lower right). The black horizontal line at 34 degrees N latitude denotes the area used in the panel (i) time-longitude section. (i) Time-longitude plot of forecast and observed dryline locations at 34 degrees N latitude from 0000 UTC 24-25 May 2011.



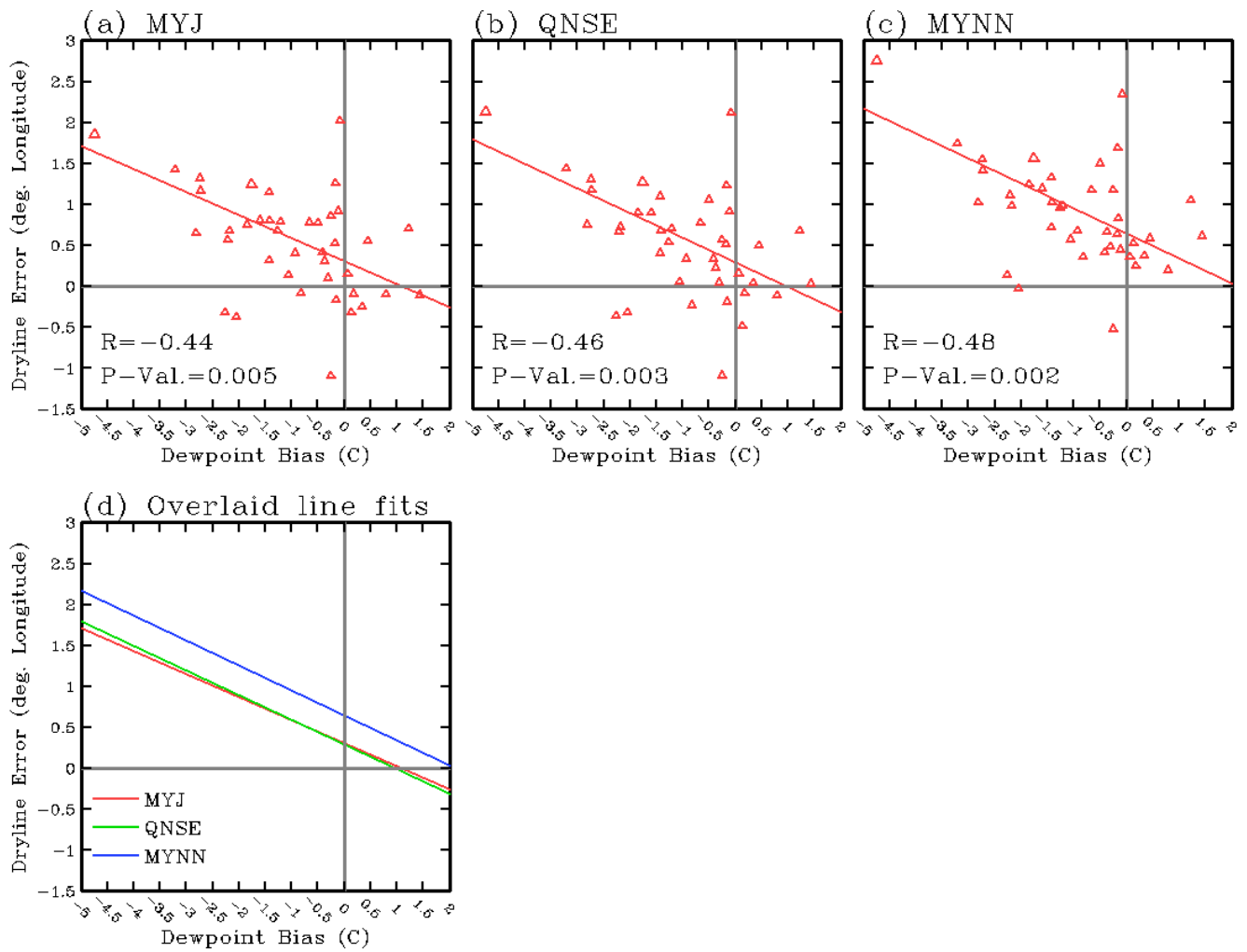
1124
 1125
 1126
 1127
 1128
 1129
 1130
 1131
 1132
 1133

Figure 5 Dewpoint (shaded; F) valid 0000 UTC 24 May 2011 (forecast hour 0) from the (a) RUC analysis, (b) MYJ without 3DVAR data assimilation, and (c) MYJ with 3DVAR data assimilation. (d) Dewpoint difference between MYJ without 3DVAR data assimilation and the RUC analysis, and (e) dewpoint difference between MYJ with 3DVAR data assimilation and MYJ without 3DVAR data assimilation. (f) – (j), (k) – (o), (p) – (t), and (u) – (y), same as (a) – (e) except valid at forecast hours 3, 6, 12, and 18 respectively.

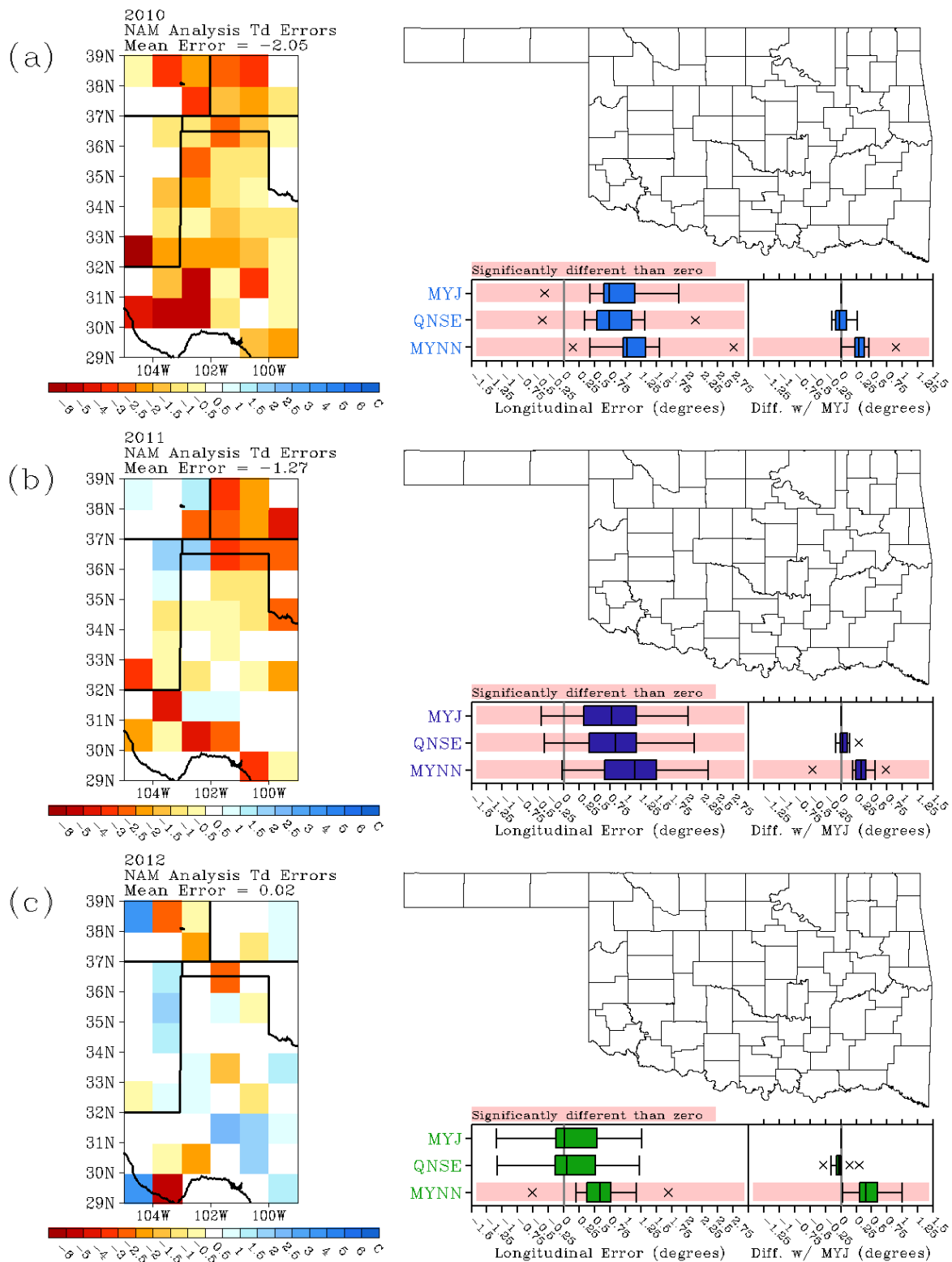


1134

1135 Figure 6 Box plots for the distribution of average longitudinal dryline position errors for the sets of cases
 1136 covering 2010-2012, 2011-2012, and 2011-only (left side). The right side box plots are for the differences
 1137 in dryline position with respect to MYJ. The interquartile range (IQR) within each box plot is colored
 1138 according to the particular boundary layer scheme (indicated on y-axis). The under-laid pink shading
 1139 indicates that differences with respect to the observations (left side) or MYJ (right side) were statistically
 1140 significant at $\alpha = 0.05$. The median is indicated by the straight black line through each box, the box
 1141 encompasses the IQR, outliers defined by values outside of $1.5 \times$ IQR are marked by crosses, and
 1142 horizontal lines (whiskers) denote the smallest and largest values that are not outliers. The map of
 1143 Oklahoma is shown for reference – its horizontal scale matches that of the x-axis for the box plots.
 1144



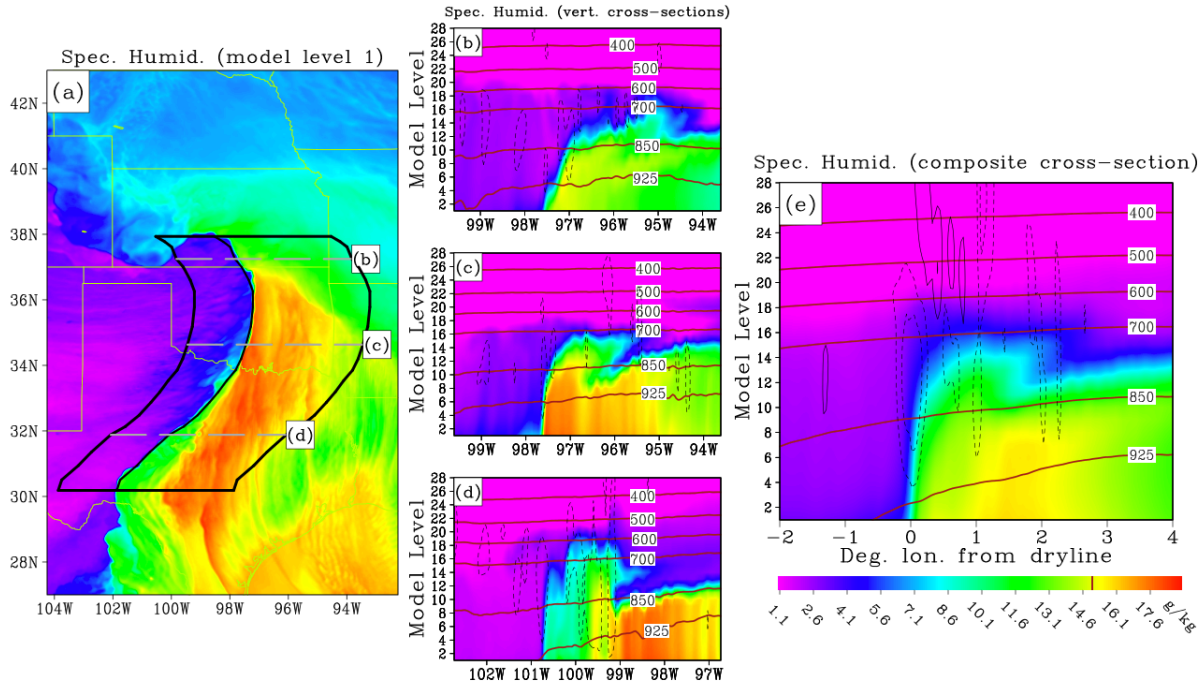
1145
 1146 Figure 7 Scatterplots of average 2-m dewpoint bias in the NAM initial conditions for the area bounded
 1147 by -105 to -99 degrees west longitude and 29 to 39 degrees north latitude versus average
 1148 longitudinal dryline error for (a) MYJ, (b) QNSE, and (c) MYNN. The red lines show the “best
 1149 fit” computed using linear regression. Correlation coefficients (R) are shown at the bottom left
 1150 along with the corresponding p-values. (d) Overlay of best fit lines from (a), (b), and (c).
 1151
 1152
 1153
 1154
 1155
 1156
 1157
 1158
 1159
 1160
 1161
 1162
 1163
 1164
 1165



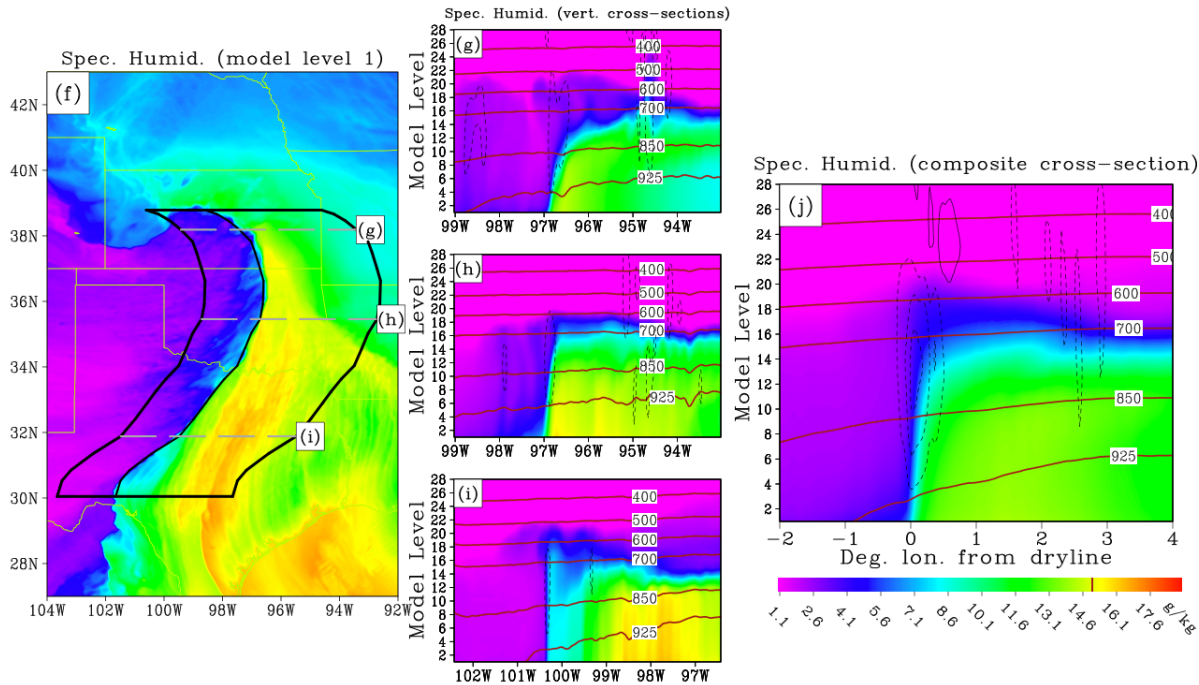
1166
 1167
 1168
 1169
 1170
 1171
 1172

Figure 8 (a) On the left, mean 2-m dewpoint errors in the NAM ICs for the 2010 dryline cases. On the right, box plots for the distribution of average longitudinal dryline position errors for the 2010 cases. The box plots are constructed similarly to those in Figure 6. (b) and (c) same as (a) except for the years 2011 and 2012, respectively.

MYJ COMPOSITE EXAMPLE – 0000 UTC 11 May 2010



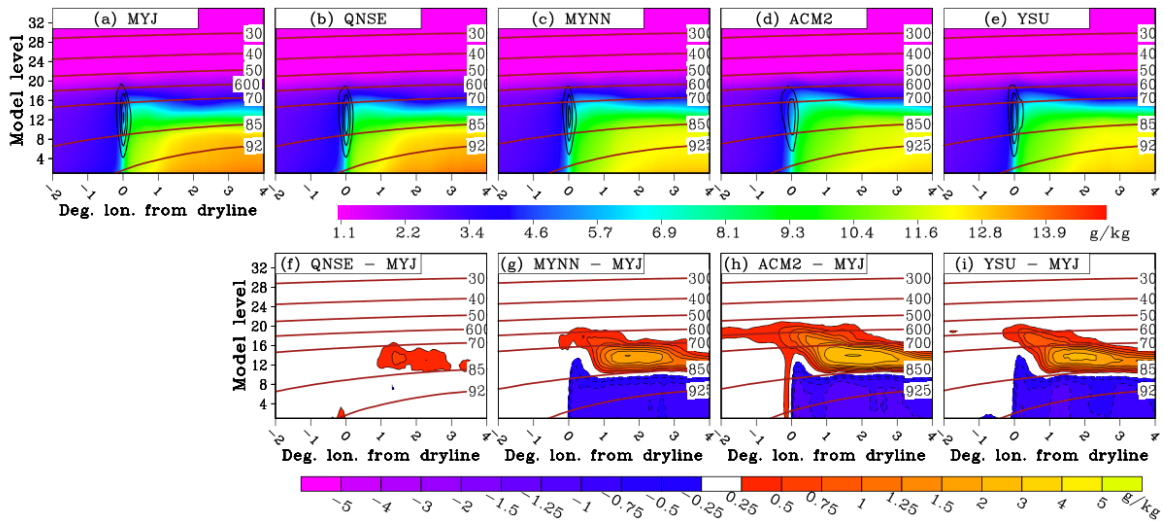
MYNN COMPOSITE EXAMPLE – 0000 UTC 11 May 2010



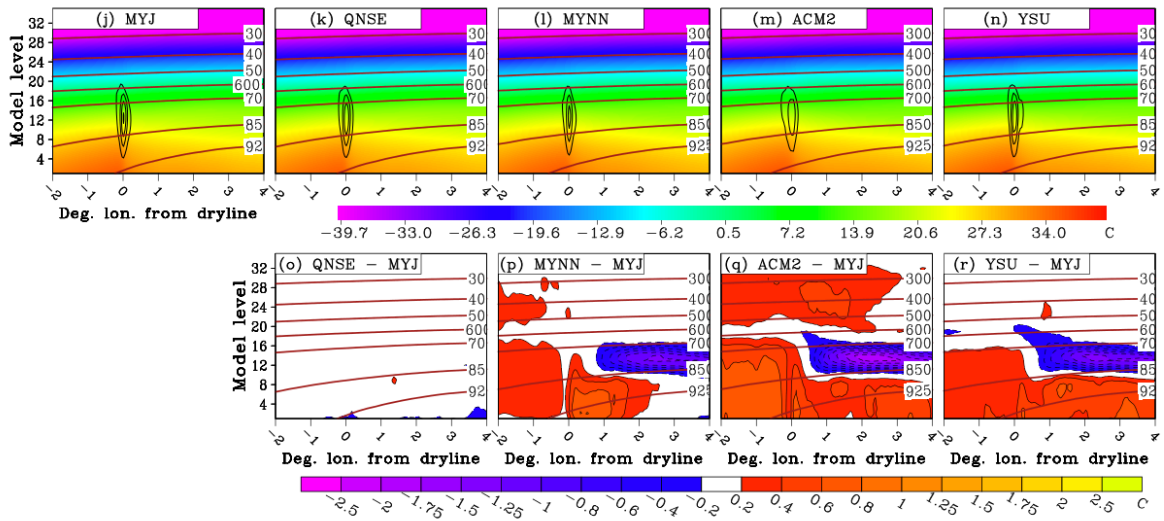
1173
1174
1175
1176
1177
1178
1179
1180
1181

Figure 9 (a) Specific humidity (shaded; kg/kg) at the lowest model level in the 24 h forecast from the MYJ member valid 0000 UC 11 May 2010. The area enclosed by the thick black line is the area over which a composite dryline cross-section was constructed. The thin black line inside of this area marks the dryline. The horizontal gray dashed lines within the area that are marked (b), (c), and (d) show the location of individual vertical cross sections of specific humidity (shaded) and pressure (red contours) in panels (b), (c), and (d). (e) Composite vertical cross section of specific humidity and pressure constructed by taking the average of cross sections anchored every 0.15 degrees latitude along the dryline. (f) – (j) same as (a) – (e), except for the MYNN member.

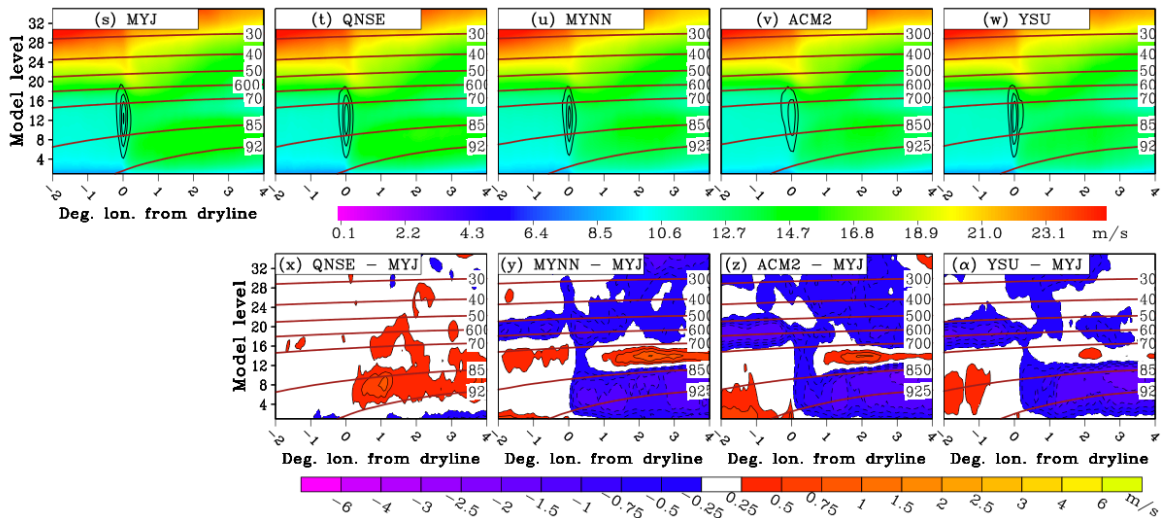
SPECIFIC HUMIDITY



TEMPERATURE



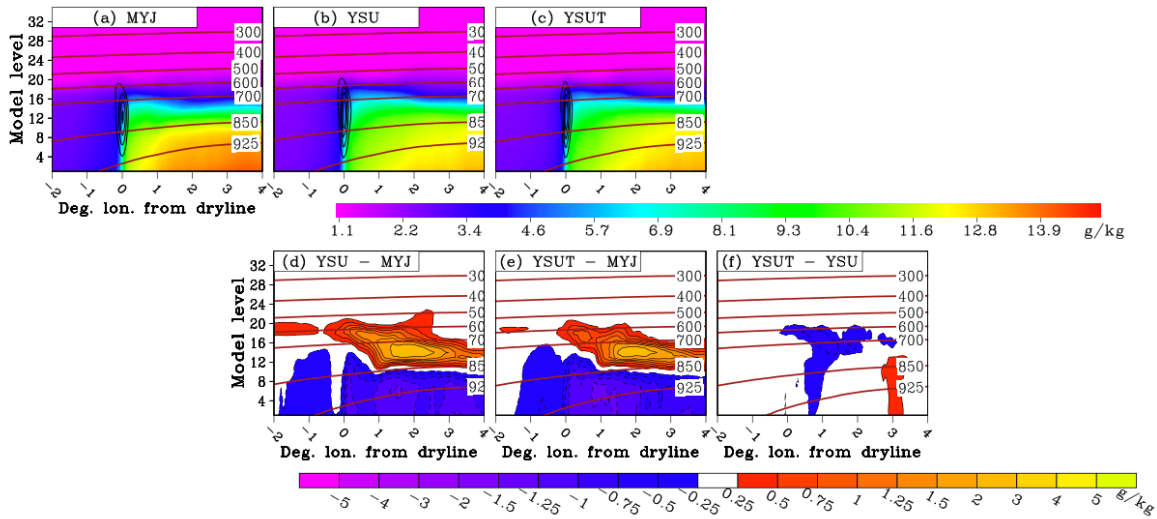
WIND MAGNITUDE



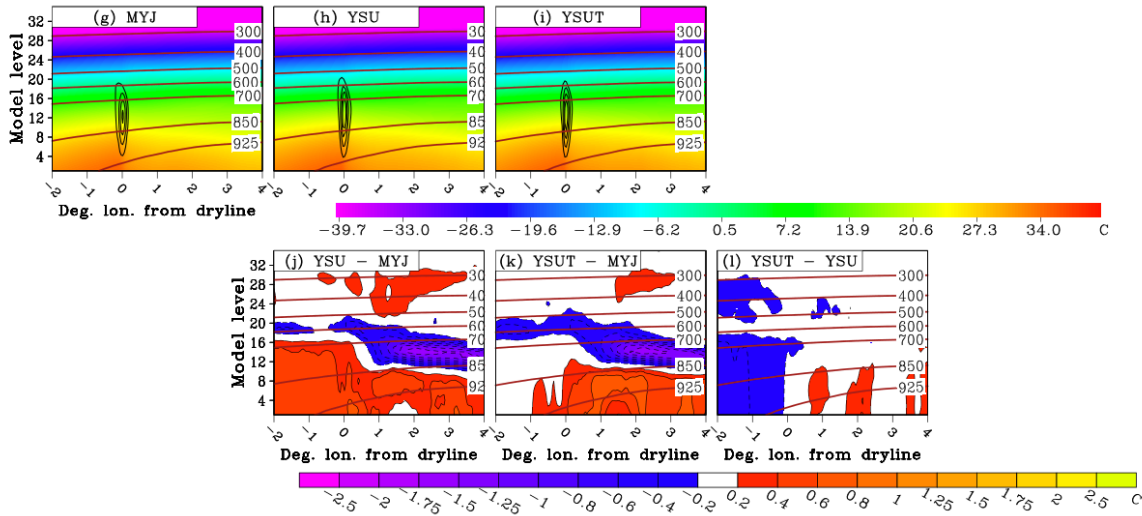
1182
1183
1184
1185
1186
1187
1188

Figure 10 Composite vertical cross sections of specific humidity (shaded; g/kg), pressure (red contours; mb) and upward vertical velocity (black contours at 1 Pa s^{-1} increments from -1 to -6 Pa s^{-1}) over all 2011-2012 cases for (a) MYJ, (b) QNSE, (c) MYNN, (d) ACM2, (e) YSU. Pressure (red contours) and specific humidity difference relative to MYJ (shaded) for (f) QNSE, (g) MYNN, (h) ACM2, and (i) YSU. (j) – (r) and (s) – (α) same as (a) – (i) except for temperature and wind magnitude, respectively.

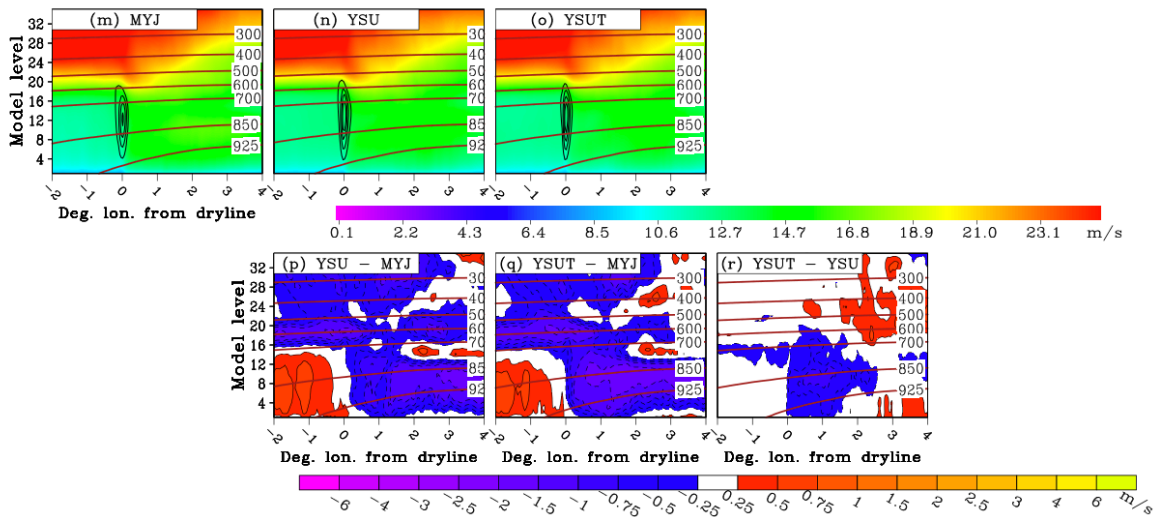
SPECIFIC HUMIDITY



TEMPERATURE



WIND MAGNITUDE



1189
1190
1191
1192
1193
1194
1195

Figure 11 Composite vertical cross sections of specific humidity (shaded; g/kg), pressure (red contours; mb) and upward vertical velocity (black contours at 1 Pa s^{-1} increments from -1 to -6 Pa s^{-1}) over all 2011 cases for (a) MYJ, (b) YSU, and (c) YSU-T. Pressure (red contours) and specific humidity difference relative to MYJ (shaded) for (d) YSU and (e) YSU-T. (f) Specific humidity difference between YSU and YSU-T. (g) – (l) and (m) – (r) same as (a) – (f) except for temperature and wind magnitude, respectively.

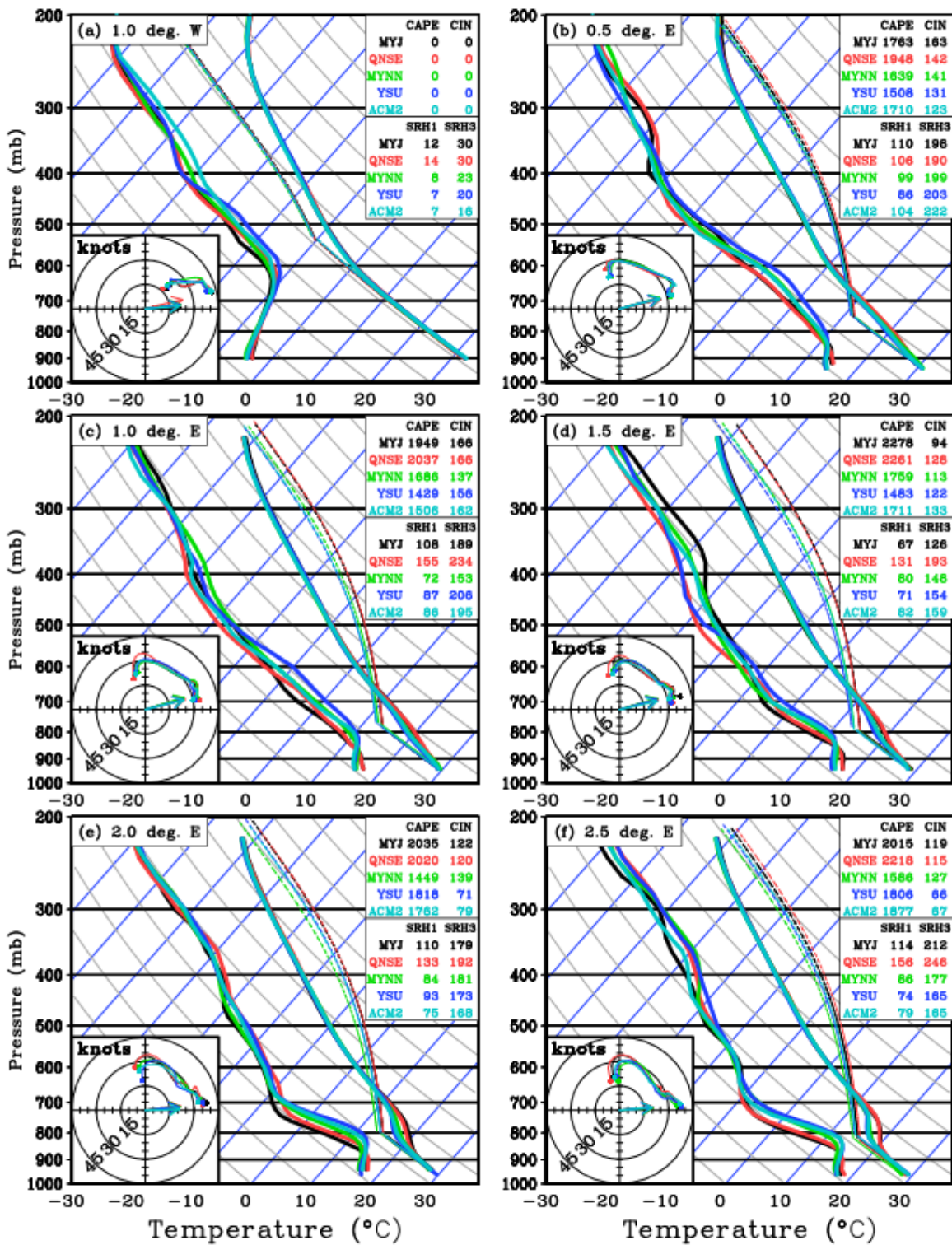
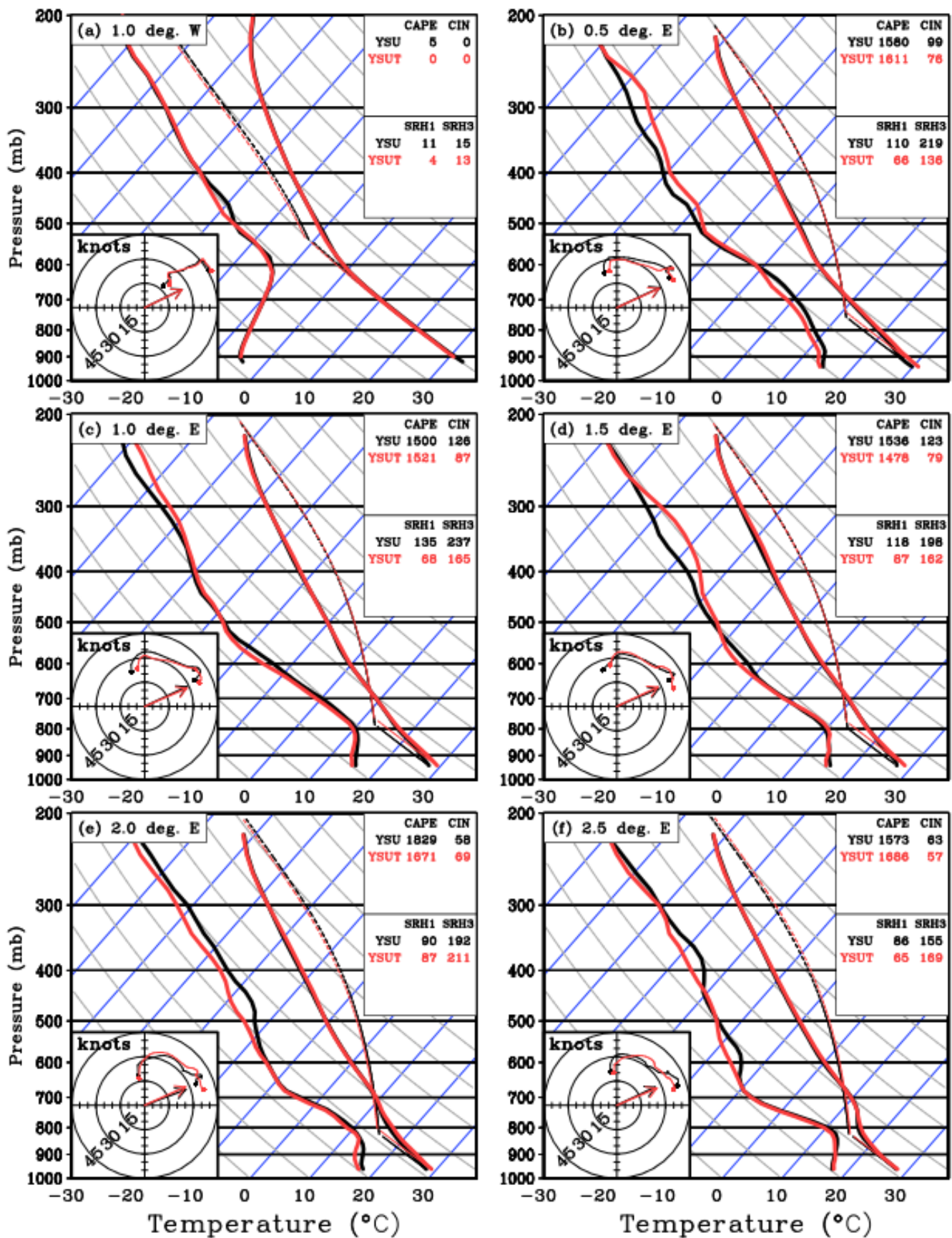
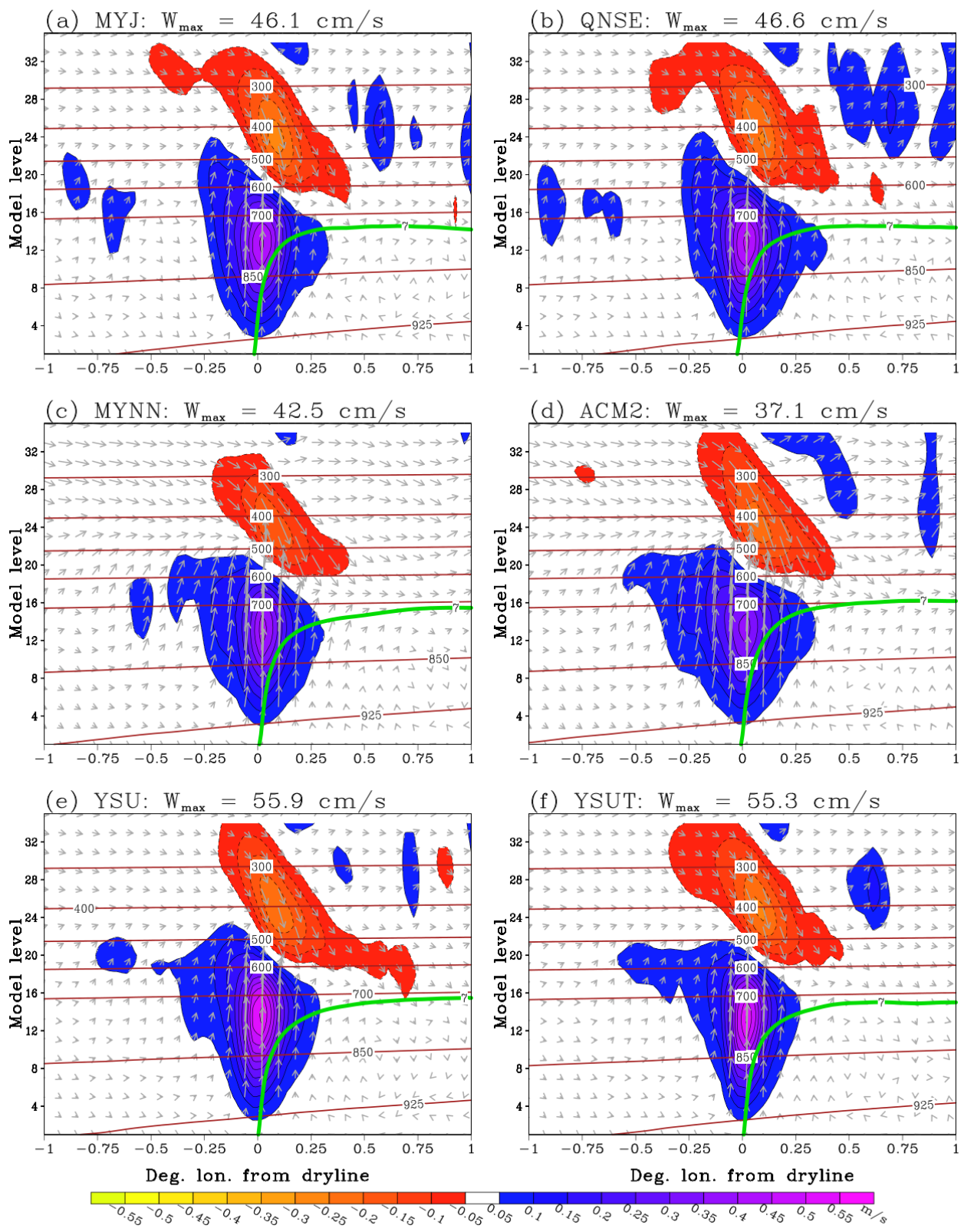


Figure 12 Dryline-relative composite soundings and hodographs over the lowest 800 mb of each profile from MYJ, QNSE, MYNN, YSU, and ACM2 for the 2011-2012 (30 cases). Solid lines depict the temperature and dewpoint traces, and the dashed lines trace the path of surface-based air parcels. The north-south “anchor point” of the composite soundings was found by following the dryline 1 degree south from its northernmost point. Then, the composites were constructed by taking averages over all cases at the following distances relative to the dryline anchor point: (a) 1.0 degrees west, (b) 0.5 degrees east, (c) 1.0 degrees east, (d) 1.5 degrees east, (e) 2.0 degrees east, and (f) 2.5 degrees east. CAPE, CIN, and Storm-relative helicity over the bottom 100 and 300 mb layers (SRH1 and SRH3, respectively) are shown for each member at the top-right of each panel. The text color of each member corresponds to the color of each member’s temperature and dewpoint trace. In the hodographs the storm motion vector is shown, which was computed following Davies-Jones et al. (1990).



1207
1208
1209

Figure 13 Same as Figure 12, except profiles are from YSU and YSUT for the 2011 drylines (14 cases).



1210
 1211
 1212
 1213
 1214
 1215
 1216

Figure 14 Dryline-relative composite vertical velocity magnitude (shaded; m/s) for 2011 (14 cases). Wind vectors depict the u and w components with the w-component multiplied by a factor of 50 to emphasize the vertical component. Pressure (hPa) is shown by the dark red contours. The 7 kg/kg specific humidity contour (green) is shown to delineate the moist sector. The maximum vertical velocity in each cross section is provided at the top of each panel. Each panel displays a different PBL member: (a) MYJ, (b) QNSE, (c) MYNN, (d) ACM2, (e) YSU, and (f) YSUT.